Materials Today Bio 27 (2024) 101156

Contents lists available at ScienceDirect

Materials Today Bio

journal homepage: www.journals.elsevier.com/materials-today-bio

Photothermal driven BMSCs osteogenesis and M2 macrophage polarization on polydopamine-coated Ti_3C_2 nanosheets/poly(vinylidene fluoride trifluoroethylene) nanocomposite coatings

Sanqiang Xia [a,b,1], Dun Liu [c,1], Kanling Jiang [b], Miao Cao [a], Zhenqi Lou [b], Ruobing Cheng [a], Jie Yi [a], Anlin Yin [a], Yi Jiang [b], Kui Cheng [d], Wenjian Weng [d], Benlong Shi [c,**], Bolin Tang [a,e,*]

[a] School of Materials and Textile Engineering, Jiaxing University, Jiaxing, 314001, China
[b] The Affiliated Hospital of Jiaxing University, Jiaxing, 314001, China
[c] Division of Spine Surgery, Department of Orthopedic Surgery, Affiliated Drum Tower Hospital, Medical School of Nanjing University, Nanjing, 210008, China
[d] School of Materials Science and Engineering, State Key Laboratory of Silicon Materials, Zhejiang University, Hangzhou, 310027, China
[e] Nanotechnology Research Institute, G60 STI Valley Industry & Innovation Institute, Jiaxing University, Jiaxing, 314001, China

ARTICLE INFO

Keywords:
Bioactive coating
MXene
Photothermal
Osteogenesis
Immunoregulation

ABSTRACT

Mild thermal stimulation plays an active role in bone tissue repair and regeneration. In this work, a bioactive polydopamine/Ti_3C_2/poly(vinylidene fluoride trifluoroethylene) (PDA/Ti_3C_2/P(VDF-TrFE)) nanocomposite coating with excellent near-infrared light (NIR)-triggered photothermal effect was designed to improve the osteogenic ability of implants. By incorporating dopamine (DA)-modified Ti_3C_2 nanosheets into the P(VDF-TrFE) matrix and combining them with alkali initiated in situ polymerization, the resulting PDA/Ti_3C_2/P(VDF-TrFE) nanocomposite coating gained high adhesion strength on Ti substrate, excellent tribological and corrosion resistance properties, which was quite important for clinical application of implant coatings. Cell biology experiments showed that NIR-triggered mild thermal stimulation on the coating surface promoted cell spreading and growth of BMSCs, and also greatly upregulated the osteogenic markers, including Runt-Related Transcription Factor 2 (RUNX2), alkaline phosphatase (ALP), osteopontin (OPN), osteocalcin (OCN). Simultaneously, the synthesis of heat shock protein 47 (HSP47) was significantly promoted by the mild thermal stimulation, which strengthened the specific interaction between HSP47 and collagen I (COL-I), thereby activating the integrin-mediated MEK/ERK osteogenic differentiation signaling pathway. In addition, the results also showed that the mild thermal stimulation induced the polarization of macrophages towards M2 phenotype, which can attenuate the inflammatory response of injured bone tissue. Antibacterial results indicated that the coating exhibited an outstanding antibacterial ability against *S. aureus* and *E. coli*. Conceivably, the versatile implant bioactive coatings developed in this work will show great application potential for implant osseointegration.

1. Introduction

The injury of bone tissue caused by bone destructive diseases (bone fracture, bone tumor resection, osteonecrosis, etc.) can seriously affect the normal function of skeletal system [1]. Clinically, the implantation of biomaterials is a common way for repair and regeneration of the damaged bone tissue. By virtue of excellent mechanical performances and biocompatibility, titanium alloys have been widely used as implantation materials in orthopedic surgery, such as internal fixation plate [2]. However, the inherent bioinertness of titanium alloys often brings the low osteogenic capability and weak osseointegration, which may lead to implant failure [3]. An effective way to enhance the osteogenic activity of a bone implant is to cover its surface with a bioactive coating that can provide suitable physical or/and chemical microenvironments for cell growth, proliferation and osteogenic differentiation [4]. Nevertheless, the most of currently developed bioactive coatings still exhibit limited osteogenic potential after being implanted into body. How to enhance cellular osteogenic differentiation for rapid repair and

* Corresponding author. School of Materials and Textile Engineering, Jiaxing University, Jiaxing, 314001, China.
** Corresponding author.
E-mail address: bltang@zjxu.edu.cn (B. Tang).
[1] Authors contributed equally to this work.

https://doi.org/10.1016/j.mtbio.2024.101156
Received 25 April 2024; Received in revised form 11 July 2024; Accepted 12 July 2024
Available online 14 July 2024

regeneration of defective bone tissue remains a major challenge at present.

Temperature (thermal stimulation) is an important factor affecting bone growth and development, and many studies have shown that thermal stimulation may effectively promote cellular differentiation and bone regeneration [5,6]. Scutt et al. [7] found that the thermal stimulation at 41 °C enhanced the ALP activity and capacity of mineralization of BMSCs. Zhang et al. [8] demonstrated that the thermal stimulation at 40–43 °C can enhance the cell proliferation of MC3T3-E1 and the rate of new bone formation greatly. However, Branemark et al. [9] found that when the temperature exceeded 45 °C, the osteoblasts were irreversibly damaged along with the significantly increased activity of caspase 3 (apoptosis-promoting protease). It is generally acknowledged that mild thermal stimulation ($\Delta T \leq 5$ °C) has a pro-osteogenic effect, and the excessive temperatures can instead accelerate cell apoptosis and damage host bone tissue [10]. In the process of bone tissue regeneration, the cellular osteogenic capability is critical, but the immune response of host bone tissue to implant materials cannot be ignored. It has been revealed that the immune response driven by macrophages (a kind of heterogeneous immune cells that are widely lived in injured tissue) play an important role in bone tissue regeneration [11]. As is well known, the macrophages can be polarized towards two different phenotypes (classically activated M1 and alternatively activated M2) according to the surrounding microenvironment, and the M1 macrophages can damage host bone tissue by secreting pro-inflammatory cytokines and the M2 macrophages can accelerate the formation of new bone by secreting anti-inflammatory cytokines [12,13]. Han et al. [14] have revealed that mild thermal stimulation can promote macrophage polarization towards M2 phenotypes. Therefore, designing biomaterials with mild thermal stimulation effect should be a feasible way to modulate cellular osteogenic differentiation and macrophage polarization, two crucial processes in bone regeneration.

In recent years, NIR-responsive photothermal materials have received increasing attention in different biological areas, such as tissue regeneration and cancer therapy, by virtue of the large tissue penetration depth, spatiotemporal tunability and biosafety of NIR [15,16]. In particular, the polymer photothermal composites composed of polymer matrix and photothermal nanofillers have been widely studied in bone regeneration [17–19]. P(VDF-TrFE) is a kind of fluoropolymer with excellent biocompatibility and physiological stability, and has been proved to support cell growth and bone regeneration in our previous works and other publications [20–23]. As a member of the MXene family, Ti_3C_2 nanosheets possess a near 100 % NIR photothermal conversion efficiency and excellent biocompatibility [24]. It is speculated that the Ti_3C_2 nanosheets reinforced P(VDF-TrFE) nanocomposite coating will gain excellent photothermal property, which can be used for promoting bone regeneration. However, the low adhesion strength of the Ti_3C_2/P(VDF-TrFE) coating on titanium implant makes it easy to fall off after being implanted into the body, which will cause the coating to lose its function, thereby resulting in implantation failure. Inspired by the mussel's adhesive proteins, polydopamine (PDA) has emerged as a powerful tool for improve interfacial adhesion strength due to the strong interaction of PDA catechol groups with various surfaces [25]. Nevertheless, previous work has often involved coating the nanomaterials with PDA first and then adding PDA modified nanomaterials into the matrix to improve adhesion to different surfaces [26,27]. This approach consumes a portion of the catechol groups during modifying the nanomaterials, which may lead to subsequent weakening of the adhesion strength to other surfaces [28].

In this study, a PDA/Ti_3C_2/P(VDF-TrFE) nanocomposite coating were prepared by incorporating DA-modified Ti_3C_2 nanosheets into the P(VDF-TrFE) matrix first and then initiating in situ polymerization of DA inside matrix. The adhesion strength, tribological and corrosion resistance properties of the PDA/Ti_3C_2/P(VDF-TrFE) coating were investigated, which is quite important in the clinical application of bone implants. The osteogenic differentiation of BMSCs and polarization behaviors of macrophages on the coating were further investigated, and the underlying photothermal osteogenic mechanism were explored. Considering that bacterial infection can hinder the osseointegration between host bone tissue and implant, the photothermal antibacterial activity of the coatings were also tested. The photothermal coatings developed in this work may provide important guidance for the surface design and modification of bone implants.

2. Materials and methods

2.1. Materials

Ti_3AlC_2 powders (400 mesh) were purchased from Jiaxing Hesimo New Material Technology Co., LTD. (Jiaxing, China), and P(VDF-TrFE) (70/30) powders were obtained from Piezotech (France). Dopamine hydrochloride (DA), Tetramethylammonium hydroxide pentahydrate (TMAH), Tris(hydroxymethyl)metyl aminomethane (Tris), N,N-dimethylformamide (DMF), HF (40 %), concentrated HCl (37 %), concentrated HNO_3 (68 %), NaOH (AR), acetone and absolute ethanol were supplied from Sinopharm Chemical Reagent Co. Ltd. (Shanghai, China). Ti substrates (Ti6Al4V alloy, 10 × 10 × 1 mm in dimensions) were provided by Taizhou Huihuang new materials Co. Ltd. (Taizhou, China). All reagents are analytical grade without further purification.

2.2. Preparation PDA/Ti_3C_2/P(VDF-TrFE) nanocomposite coatings

The clean Ti substrates were obtained according to the reported method in our previous publication [23], and the Ti_3C_2 nanosheets solution were prepared through three procedures, i.e., the etching of Ti_3AlC_2 with HF solution, the intercalation of multilayered Ti_3C_2 with TMAH solution and the delamination of intercalated multilayered Ti_3C_2 with the assistance of ultrasound, as described in our previous work [29]. For preparation of DA/Ti_3C_2, the Ti_3C_2 nanosheets solution was firstly adjusted to pH = 5 with 1 M HCl, and then the designed amount of DA powders was added into Ti_3C_2 nanosheets solution. After stirring magnetically for 12 h, the DA/Ti_3C_2 powders were obtained through vacuum filtration with polypropylene filter membrane (pore size: 0.22 μm). The PDA/Ti_3C_2/P(VDF-TrFE) nanocomposite coatings were prepared according to the following steps: Firstly, the desired amount of DA/Ti_3C_2 powders were ultrasonically dispersed into DMF for 3 h, followed by the P(VDF-TrFE) were added into Ti_3C_2 dispersion and stirring magnetically for 3 h under supersonic vibration. Subsequently, the DA/Ti_3C_2/P(VDF-TrFE) mixed solution was casted onto the clean Ti substrates. With complete evaporation of DMF at room temperature (RT), the DA/Ti_3C_2/P(VDF-TrFE) nanocomposite coatings were obtained. After soaked in Tris buffer solution (pH = 8.5) for 24 h and then annealing crystallization for 1 h at 210 °C, the PDA/Ti_3C_2/P(VDF-TrFE) nanocomposite coatings (named as PTP-x, x represents the weight content of Ti_3C_2 nanosheets) were prepared. As contrast, the Ti_3C_2/P(VDF-TrFE) nanocomposite coatings (denoted as TP-x) and pure P(VDF-TrFE) coating (signed as PP) were also prepared with similar solution casting method as PTP-x. To obtain PDA/Ti_3C_2 nanoparticles for characterization, the PDA/Ti_3C_2 nanoparticles were separated from PDA/Ti_3C_2/P(VDF-TrFE) nanocomposite coatings through dissolving P(VDF-TrFE) matrix with DMF.

2.3. Characterizations

The surface morphology of all the samples was investigated by field-emission scanning electron microscope (FE-SEM, Apreo S, Thermo Scientific, USA) and transmission electron microscope (TEM, Talos F200X, Thermo Scientific, USA). The element mapping of PDA/Ti_3C_2 were characterized through dark field modes of TEM. The thickness, surface topography and roughness of the samples were investigated by atomic force microscope (AFM, MultiMode 8, Bruker, Gemany) at a frequency of 49 kHz and an amplitude of 0.5 V. Phase composition of the samples

was analyzed with X-ray diffractometer (XRD, D8A25, Bruker, Gemany) using Cu Ka radiation source (k = 1.54 Å) at 35 kV in the 2θ range of 10–80° with a scan rate of 5°/min. Fourier transform infrared (FTIR) spectra of the samples were recorded by an infrared spectrometer (Vertex 70, Bruker, Gemany) with the range from 400 cm^{-1} to 4000 cm^{-1} at room temperature, and ultraviolet–visible (UV–vis) absorption spectra of the samples were recorded by an ultraviolet–visible spectrophotometer (Evolution 350, Thermo Scientific, USA). The chemical composition was tested by X-ray photoelectron spectroscopy (XPS, Escalab 250Xi, Thermo Scientific, USA) with Mg Kα source at a base pressure of 3.5×10^{-9} Torr. Thermogravimetric analysis (TGA) of the samples was carried out by a thermal gravimetric analyzer (Q50, TA Instruments, USA) at a heating rate of 5 °C/min from 30 to 800 °C under a nitrogen atmosphere. The surface potential of Ti_3C_2 nanosheets was measured with a zeta potential analyzer (Zetasizer Nano ZSE, Malvern Instruments, England) from pH 4 to 10 adjusted with 0.1 M HCl and NaOH solutions. The surface wettability of the samples was measured by contact angle meter (DSA30, Kruss, Gemany) equipped with a CCD camera, and the equilibrium state of the water droplet upon contact with the coating surface was used as contact angle.

2.4. Elastic modulus, indentation hardness and adhesion strength of coatings

The elastic modulus, indentation hardness and adhesion strength of the coating samples were tested at room temperature by a micro/nano-mechanical properties test system (UNHT3-NST3, Anton Paar, Austria). The elastic modulus and indentation hardness were calculated by Oliver-Pharr method based on the load-displacement curves obtained from nanoindentation experiments [30], in which a diamond indenter (type: Berkovich; serial number: BBF-48) was used, and the maximum load, loading/unloading rate and load holding time were set to 50 mN, 100 mN/min and 10 s, respectively. The adhesion strength of coatings on substrate was examined via nano-scratch test, in which a diamond indenter (Radius: 2 μm; type: Spherical; serial number: SB-C87) was adopted, and the begin load, end load, force increasing rate, scratch length were set as 10 mN, 500 mN, 10 mN/s and 0.5 mm, respectively. The critical load (defined as the smallest load when a recognizable failure of a coating occurs, which was observed using an optical microscope) is considered to be the adhesion strength of coatings on substrate [31].

2.5. Tribological property tests

The friction coefficient (μ) and wear rate of the coating samples were tested at room temperature (relative humidity: 60 %) by a multifunctional friction and wear testing machine (TRB3, Anton Paar, Austria) with ball-on-plate module under linear reciprocating mode. The stainless steel ball with a diameter of 5 mm was used as rolling ball, and the normal load, sliding distance, sliding speed and number of reciprocating motion were set to 5 N, 5 mm, 1 cm/s and 200, respectively. The μ was calculated as the average value over the entire test period, and the wear rate was calculated according to formula W=V/(F*L), where W, V, F, and L are the wear rate, wear volume, normal load, and sliding distance, respectively [32].

2.6. Electrochemical corrosion tests

The corrosion resistance property of the coating samples in SBF solution were assessed via an electrochemical workstation (CHI760E, Chenhua Instrument Co., Ltd, Shanghai, China). The electrochemical tests were conducted with a three-electrode system. The working electrode was the coating/Ti samples, and the counter electrode and reference electrode were platinum plate and silver chloride electrode. Before the measurement, those samples were immersed in SBF solution for 30 min to obtain a steady state open-circuit potential (OCP). Electrochemical impedance spectroscopy (EIS) tests were recorded under the OCP value with the frequency ranging from 100 kHz to 0.01 Hz. The polarization curves were recorded with the potential ranging from −1500 to +1000 mV and the scan rate of 1 mV/s. The EIS data were fitted by ZsimpWin software to provide further explanation about the corrosion resistance of coating samples in SBF solution. The corresponding corrosion potential (E_{corr}) and corrosion current density (i_{corr}) were also analyzed by Tafel linear extrapolation.

2.7. Photothermal performance studies

The photothermal performance of the coating samples was investigated with an infrared camera (Haikang H10). The coating samples were immersed into PBS solution (1 mL), followed by irradiated with 808 nm NIR for 10 min. The temperature of the coating samples was recorded at an interval of 30 s (initial temperature: ~20 °C). To test the photothermal performance of the coating samples under the environment of 37 °C, the initial temperature of 37 °C was maintained using a thermostat water bath.

2.8. Isolation of bone marrow mesenchymal stem cells (BMSCs) and cell culture

As previously described, BMSCs were extracted from the bone marrow of 4-week-old male Sprague Dawley (SD) rats. After separating the surface muscles from the femur and tibia of the rats, the bone ends were cut open to expose the bone marrow cavity, followed by rinsing. Once thoroughly rinsed, the cell suspension containing the bone marrow was collected in a 15 mL centrifuge tube and repeatedly pipetted using a 1 mL pipette until no visible cell clumps were present, followed by centrifugation to remove the supernatant. The aforementioned cells were then placed in an incubator at 37 °C with 5 % CO_2, and the culture medium (α-MEM+10%FBS+0.5%Penicillin-streptomycin) was changed every 2–3 days.

2.9. Cell viability assessment

The biocompatibility of PDA/Ti_3C_2/P(VDF-TrFE) nanocomposite coating was evaluated using Live/Dead staining kits. BMSCs were cultured on samples with different surface modifications for 48 h. An 808 nm NIR was illuminated on each sample for 10 min, conducted once daily. Live cells were stained green with calcein-AM, while dead cells were stained red with propidium iodide. Fluorescent images were captured using a microscope. The effect of PDA/Ti_3C_2/P(VDF-TrFE) nanocomposite coatings on cell viability of BMSCs was detected by CCK-8 kits. Following the instructions in the user manual, the absorbance at 450 nm of each group was measured using a microplate reader after the addition of the CCK-8 working solution. Cell survival was calculated as the percentage of absorbance of cells cultured on the coatings relative to the control (culture dish).

2.10. Cell adhesion assay

BMSCs were seeded on the surfaces of each nanocomposite coating and treated according to the group. An 808 nm NIR was illuminated for 10 min, conducted once daily. After co-culturing for 48 h, the cells were fixed with 4 % paraformaldehyde and stained with rhodamine-labeled phalloidin for F-actin staining for 30 min. The cell nuclei were stained with DAPI. Finally, fluorescent images were obtained with a microscope, and the cell spreading area, perimeter, and Feret's diameter were quantitatively analyzed using Image J software.

2.11. Osteogenic activity assay

In order to evaluate the effects of different coatings and NIR-mediated mild thermal stimulation on osteogenic differentiation of

BMSCs in vitro, we used osteogenic medium composed of 50 μg/mL ascorbic acid 2 phosphate, 10 mM glycerol β-glycerophosphate and 0.1 μM dexamethasone to induce osteogenic differentiation of BMSCs. During culture, the cells were irradiated for 10 min daily by 808 nm NIR according to the group. After 14 days of culture, alkaline phosphatase (ALP) activity was detected by ALP staining kits, and mineralization was evaluated by alizarin red staining kits. When the fusion degree of BMSCs cultured on the sample reached 90 %, the protein was extracted using total protein extraction kits, and the expression of osteogenic marker proteins osteopontin (OPN), recombinant runt related transcription factor 2 (RUNX-2) and osteocalcin (OCN) were quantitatively detected by Western blotting. The steps of Western blotting are briefly described as follows: First, the total protein extraction kit was used to extract the proteins of each group and the bicinchoninic acid assay (BCA) kit was used for quantitative analysis of the proteins. The protein samples were added to 10 % PAGE gel for electrophoresis, and the voltage was adjusted to 120 V after maintaining a constant voltage of 80 V for 30 min. PVDF was used for transmembrane and subsequently sealed with skim milk powder. Dilute of different primary antibodies were added and incubated overnight. After rinsing thoroughly, the corresponding secondary antibodies were added for incubation. Finally, a chemiluminescence kit was used for protein band development photography. In addition, the expression of osteoblast-related protein OPN was evaluated by immunofluorescence staining. The steps of immunofluorescence staining are briefly described as follows: First, the cells were fixed with 4 % paraformaldehyde for 10 min and then infiltrated with 0.3 % Triton-X for 10 min. After soaking with serum sealer, different antibodies were added and kept in refrigerator at 4 °C overnight. Fluorescent secondary antibody was then added and the nucleus was stained with DAPI solution. Finally, confocal microscope was used to observe and photograph.

2.12. Mechanism of osteogenic differentiation induced by the composite coating combined with NIR

To elucidate the mechanism of photothermal driven osteogenesis by PDA/Ti_3C_2/P(VDF-TrFE) nanocomposite coating, Western blotting was used to detect the expression of heat shock protein 47 (HSP-47), COL-I, integrin-α2, integrin-β1 and key proteins in the MEK/ERK signaling pathway in each group. In the inhibition test, the 10 μM U0126 (an inhibitor of the MEK/ERK signaling pathway) was added into the culture system with other culture conditions at the same.

2.13. Macrophage polarization in vitro assessment

To evaluate the effects of composite coatings and mild thermal stimulation on macrophage polarization, RAW264.7 cells were cultured on different surfaces, and their M1 phenotype was induced by hydrogen peroxide solution. During culture, the cells were irradiated for 10 min daily by 808 nm NIR according to the group. After 3 days of co-culture, the expression of M1 macrophage associated marker (Inducible nitric oxide synthase, iNOS) and M2 macrophage associated marker (Arginase 1, Arg-1) was evaluated by immunofluorescence staining and Western blotting, respectively. In addition, the culture medium supernatant was collected and the secretion of inflammatory factors tumor necrosis factor-α (TNF-α), iNOS, Arg-1 and interleukin-10 (IL-10) was analyzed by enzyme-linked immunosorbent assay (ELISA) kits.

2.14. Antioxidant capacity test

To evaluate the antioxidant capacity of the PDA/Ti_3C_2/P(VDF-TrFE) nanocomposite coating, the in vitro and *vivo* ROS scavenging assays were carried out by using different free radicals (in vitro) and DCFH-DA probe (*in vivo*). Three commonly used free radicals including superoxide radical ($\cdot O_2^-$), hydroxyl radical (·OH) and DPPH radical (DPPH·) are selected for scavenging assays.

For $\cdot O_2^-$ scavenging, 1 mL of deionized water (control group), nanoparticle aqueous dispersion (2 mg mL^{-1}) or one coating sample (containing ~2 mg nanoparticles) was mixed with 12 mL of Tris-HCl (10 mM, pH 8.2). Subsequently, 500 μL of pyrogallol solution (30 mM) was added to the mixed solution for 30 min incubation under NIR (−) (in the dark) or NIR (+) (808 nm NIR irradiation for only 10 min). Then the mixture was centrifuged at 5,000 rpm for 5 min to subside excessive nanoparticles, and the UV–vis absorption spectrum of the solution was measured at 325 nm to calculate the $\cdot O_2^-$ scavenging ratio (%) according to the formula: $[(A_{control} - A_{hydrogel})/A_{control}] \times 100$ %.

For ·OH scavenging, 300 μL of H_2O_2 (1 mM) was added into 2 mL of mixed solution (consisting of 5 mM $FeSO_4 \cdot 7H_2O$ and 5 mM salicylic acid-ethanol) to initiate the reaction. After 20 min, 1 mL of deionized water (control group), nanoparticle aqueous dispersion (2 mg mL^{-1}) or one coating sample was added, and then the mixture was incubated for 30 min under NIR (−) or NIR (+). After centrifugation, the solution absorbance was measured at 510 nm to calculate the ·OH scavenging ratio (%) according to the above formula.

For DPPH· scavenging, 1 mL of deionized water (control group), nanoparticle aqueous dispersion (2 mg mL^{-1}) or one coating sample were soaked into 3 mL DPPH ethanol solution (0.1 mM) and incubating for 30 min under NIR (−) or NIR (+). After centrifugation, the solution absorbance was measured at 517 nm to calculate the DPPH· scavenging ratio (%) according to the same formula.

For the cellular ROS level test, BMSCs were inoculated on the coating surface and supplemented with a medium containing H_2O_2 (0.1 mM). During culture, the cells were irradiated for 10 min daily by 808 nm NIR according to the group. Intracellular reactive oxygen species (ROS) levels in different coating groups were detected by DCFH-DA probe after coculture for 24 h. Photographs were taken by confocal microscopy and fluorescence quantitative analysis was performed.

2.15. Antibacterial assay in vitro

Gram-negative *Escherichia coli* (ATCC 25922) and Gram-positive *Staphylococcus aureus* (ATCC 25923) were selected to test the antimicrobial capacity of each coating in conjunction with NIR. Briefly, first, 50 μL of the prepared bacterial suspension (10^6/mL) was added to the surface of the coatings and then subjected to 10 min of NIR irradiation (500 mW/cm^2). Subsequently, the bacterial suspension was diluted after rinsing the coating with 1 mL PBS solution and then the spread plate operation was carried out. The number of colony forming units (CFU) on the solid agar plates was observed after incubation in an incubator at 37 °C for 24 h. In addition, the bacteria in each group were stained with bacterial Live/dead staining kits and observed by a high-resolution microscope to assess the survival rate of the bacteria after the above treatments, in which the dead bacteria were stained with red fluorescence by PI, while the live bacteria were stained with green fluorescence by SYTO-9. Bacterial reduction rate (%) = $(C/C_0) \times 100$ %, where C is the number of dead bacteria and C_0 is the total number of dead and live bacteria.

2.16. Statistical analysis

All experimental data are expressed as mean ± standard deviations (triplicate). Statistical differences between groups were analyzed by one-way analysis of variance (ANOVA) with Tukey's post hoc test. The software SPSS 24.0 (IBM SPSS Statistics 24, IBM, NY, USA) was used. A value of $p < 0.05$ was considered statistically significant (*$p < 0.05$, **$p < 0.01$, ***$p < 0.001$).

3. Results and discussion

3.1. Preparation and characterization of PDA/Ti_3C_2 nanoparticles

The PDA/Ti_3C_2 nanoparticles were synthesized through in situ

polymerization of DA inside P(VDF-TrFE) matrix. Firstly, the multilayered Ti_3C_2 particles were prepared via HF etching, and then the Ti_3C_2 nanosheets were obtained by TMAH intercalation and ultrasonic delamination of multilayered Ti_3C_2. The DA/Ti_3C_2 nanosheets were further obtained by the electrostatic interaction of DA and Ti_3C_2 nanosheets in aqueous solution (pH = 5). Herein, the zeta potential measurement (Fig. S1) demonstrated that the prepared Ti_3C_2 nanosheets in aqueous solution (pH = 5) are negatively charged (−28.6 ± 2.65 mV), and it is well known that –NH_2 group is easily protonated to become positively charged in acidic solution. After P(VDF-TrFE) powders were

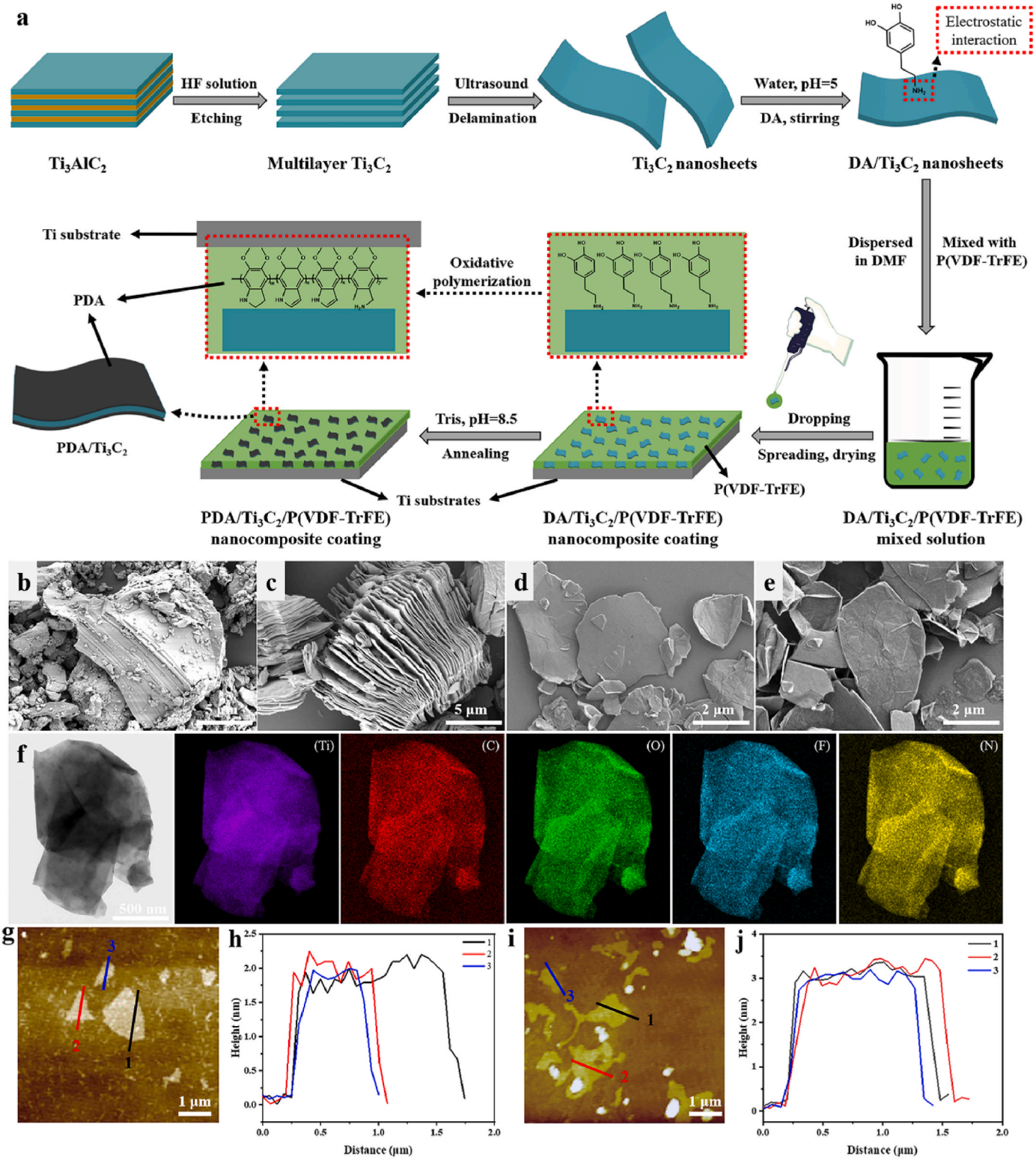

Fig. 1. Illustration for preparation of PDA/Ti_3C_2/P(VDF-TrFE) nanocomposite coatings (a). The SEM images of Ti_3AlC_2 (b), multilayered Ti_3C_2 particles (c), Ti_3C_2 nanosheets (d) and PDA/Ti_3C_2 nanoparticles (e). TEM element mapping images of PDA/Ti_3C_2 (f). AFM image (g) and thickness profile (h) of Ti_3C_2 nanosheets. AFM image (i) and thickness profile (j) of PDA/Ti_3C_2 nanoparticles.

completely dissolved in DA/Ti_3C_2 DMF dispersion, the resulted DA/Ti_3C_2/P(VDF-TrFE) solution were immediately dropped onto clean Ti substrates to prepare DA/Ti_3C_2/P(VDF-TrFE) coatings. Afterwards, the DA/Ti_3C_2/P(VDF-TrFE) coatings were soaked into Tris buffer solution to initiate the oxidative self-polymerization of DA. After the polymerization of DA was finished, the PDA/Ti_3C_2/P(VDF-TrFE) nanocomposite coating (PTP) was obtained by annealing treatment (Fig. 1a), and the PDA/Ti_3C_2 nanoparticles were finally separated from PTP with DMF solvent. The SEM images show that the Ti_3AlC_2 is a tightly stacked layered structure with a size of ~12 μm (Fig. 1b), and the typical accordion-like multilayered Ti_3C_2 is obtained by HF etching (Fig. 1c). After intercalation and ultrasonic delamination, the apparent Ti_3C_2 nanosheets were observed with quite neat surface (Fig. 1d). However, the surface of the separated PDA/Ti_3C_2 nanoparticles seem to be a little rough, maybe implying the generation of PDA via in situ polymerization of DA (Fig. 1e). TEM element mapping images (Fig. 1f) of PDA/Ti_3C_2 nanoparticles confirm that, besides the Ti, C, O, F elements, the N element is also existed in PDA/Ti_3C_2, which only derived from PDA molecules. AFM images show that the Ti_3C_2 nanosheets have visible flake structure (Fig. 1g), with a thickness of ~2.0 nm (Fig. 1h). Although the flake structure of PDA/Ti_3C_2 nanoparticles has unchanged (Fig. 1i), but its thickness has increased to ~3 nm (Fig. 1j), further implying the formation of PDA on the surface of Ti_3C_2 nanosheets.

PDA/Ti_3C_2 nanoparticles were further analyzed by other characterization methods. FTIR spectra (Fig. 2a) show that a strong adsorption band at 3430 cm^{-1} is observed in Ti_3C_2 and PDA/Ti_3C_2, which is ascribed to the stretching vibration of –OH group [29]. Compared with Ti_3C_2 nanosheets, four new weak absorption bands are found in PDA/Ti_3C_2 nanoparticles, with 1726, 1480, 1260 and 624 cm^{-1} assigned to the stretching vibration of C═O, bending vibration of indole/indoline, scissoring vibration of CH_2 and out-of-plane bending vibration of –OH of PDA, respectively [33]. UV–vis absorption spectra show that an obvious absorption peak is emerged at 231 nm (Fig. 2b), which is attributed to the light absorption of PDA [34]. XPS were further performed to analyze the elemental composition and binding states of Ti_3C_2 and PDA/Ti_3C_2. As shown in Fig. 2c, besides C, Ti, O, F elements, the N element is also detected in PDA/Ti_3C_2 nanoparticles, which only derived from PDA. The C 1s spectrum of Ti_3C_2 nanosheets has been deconvoluted into four components (Fig. 2d), with binding energies at 286.3, 285.7, 284.3 and 280.5 eV assigned to C–O, C–C, C–Ti-T_x and

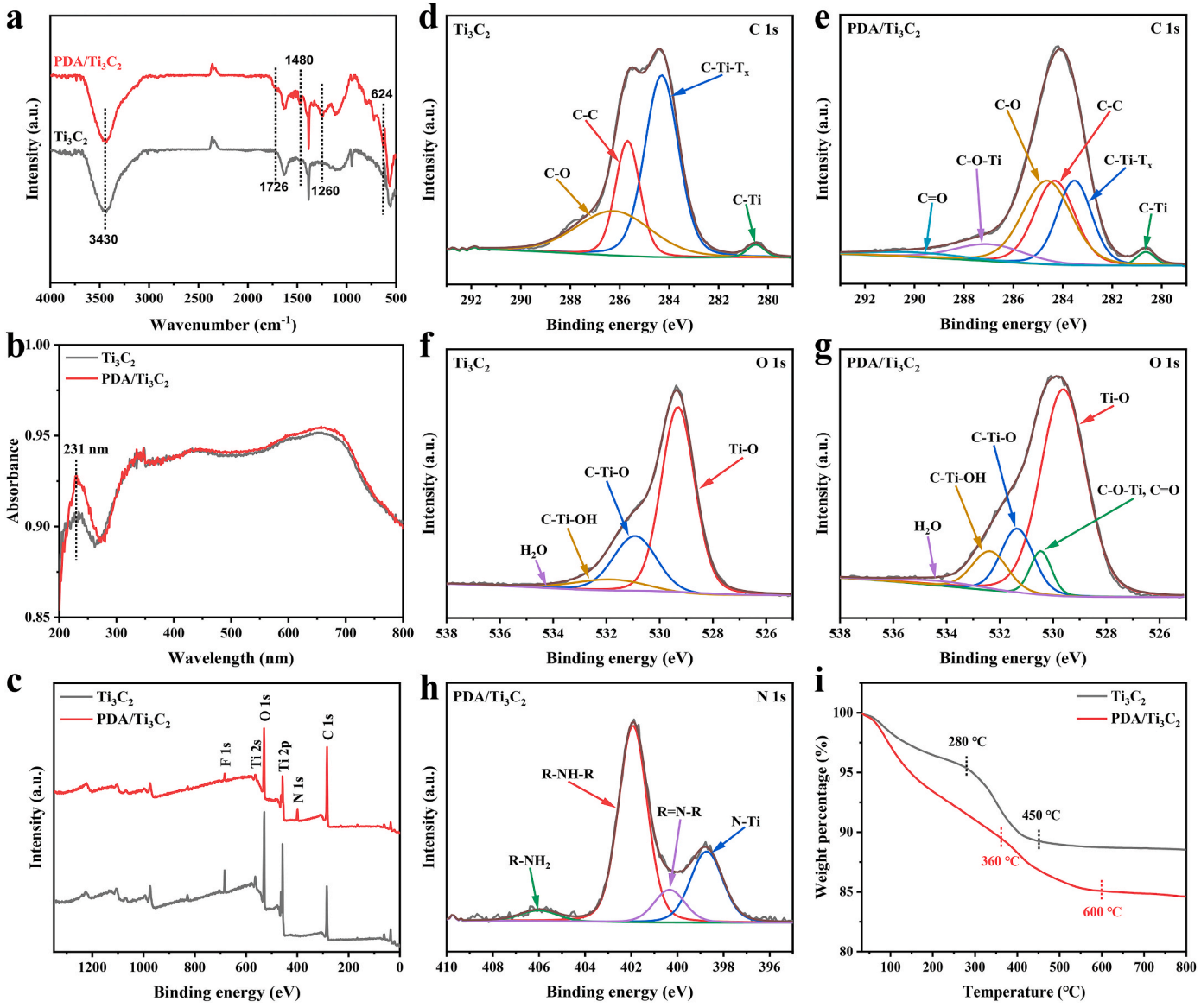

Fig. 2. FTIR spectra (a), UV–vis absorption spectrum (b), survey XPS spectra (c), C 1s (d, e), O 1s (f, g), N 1s (h) XPS fitting spectra, TGA curves (i) of Ti_3C_2 nanosheets and PDA/Ti_3C_2 nanoparticles.

C–Ti bond of Ti_3C_2, respectively. However, the deconvoluted C1s spectrum of PDA/Ti_3C_2 can be subdivided into C–O, C–C, C–Ti-T_x, C–Ti, C═O and C–O–Ti six peaks (Fig. 2e), in which the C═O at 289.3 eV and C–O–Ti at 287.2 eV originate from benzoquinonyl of PDA and the chemical bonding between phenolic –OH groups of PDA and surface Ti atoms of Ti_3C_2, respectively. For the O 1s spectrum, four deconvoluted O 1s peaks (H_2O, C–Ti–OH, C–Ti–O and Ti–O) are found in Ti_3C_2 nanosheets (Fig. 2f). However, besides H_2O, C–Ti–OH, C–Ti–O and Ti–O peaks, another overlapping peak of C–O–Ti and C═O (C–O–Ti/C═O) is identified in PDA/Ti_3C_2 nanoparticles (Fig. 2g), indicating the existence of PDA [33]. Furthermore, the N 1s spectrum of PDA/Ti_3C_2 nanoparticles is deconvoluted into four components (Fig. 2h), including R–NH_2 at 406.0 eV, R–NH–R at 401.9 eV, R═N–R at 400.4 eV and N–Ti at 398.8 eV. Herein, the R–NH–R and R═N–R bonds are indexed to the indole ring structure of PDA, and N–Ti bond is ascribed to the binding of amine at Ti atoms of Ti_3C_2 [35]. TGA curves (Fig. 2i) display that a weight loss of 4.5 % is observed in Ti_3C_2 nanosheets when the temperature is raised from room temperature to ~270 °C, which was attributed to the evaporation of the bound water adsorbed on the surface of Ti_3C_2. With the temperature raised to ~450 °C, another weight loss of 6.3 % is produced, resulting from the removal of the –OH and –F groups of Ti_3C_2 surface [36]. When the temperature exceeds 450 °C, the weight of Ti_3C_2 nanosheets almost keeps constant. The PDA/Ti_3C_2 nanoparticles presents a similar TGA curves to Ti_3C_2 nanosheets, where the first weight loss occurs at the range of room temperature to 360 °C, originating from the removal of the bound water, partial –OH and –F groups of Ti_3C_2 and thermolabile groups (-OH, –NH_2) of PDA. The second weight loss is observed at the range of 360–600 °C, which is ascribed to the elimination of the –OH and –F groups and thermal degradation of PDA [37]. It is worth noting that temperature turning points of weight loss in Ti_3C_2 and PDA/Ti_3C_2 are distinctly different, which may be attributed to the intersecting thermal degradation between Ti_3C_2 and PDA. Based on the above results and analysis, it can be concluded that the self-polymerization of DA is successfully performed inside PTP coating.

3.2. Preparation and characterization of PTP nanocomposite coatings

According to the described procedure in Fig. 1a, the PTP coatings with different Ti_3C_2 content were prepared. To screen out the optimal PTP coating for subsequent photothermal effect mediated biological studies, the photothermal property and biocompatibility of the PTP coatings with different Ti_3C_2 content were investigated. As shown in Fig. S2, the temperature elevation (ΔT) of PP, PTP-2.5, PTP-5 and PTP-10 is determined to 2.7 °C, 10.8 °C, 19.1 °C and 20.2 °C under 10 min NIR irradiation, indicating the optimal photothermal property in PTP-10. However, the live/dead staining images (Fig. S3a) and statistical results (Fig. S3b) show that the cell viability PTP-10 coating is only ~92 %, implied that the high content of Ti_3C_2 nanosheets reduced the biocompatibility of PTP coatings. It is found that the PTP-5 coating exhibits a comparable biocompatibility with control sample (blank) and nearly same ΔT as PTP-10. So, the PTP-5 was selected for subsequent coating characterization and biological studies.

Surface morphology of biomaterials has an important effect on cell behaviors. The SEM images (Fig. 3a–c) show that the PP, TP-5 and PTP-5 coatings display similar surface morphology, with large numbers of streak-like whiskers on the surface, and the thickness of PTP-5 coating is about 80 μm, determined by SEM image of cross section of PTP-5 (Fig. 3d). It can be seen from AFM images that the PP, TP-5 and PTP-5 coating present apparent undulating surface topography (Fig. 3e–g), and the averaged surface roughness are calculated to 181.7 ± 17.9 nm for PP coating, 224.8 ± 30.4 nm for TP-5 coating and 228.7 ± 43.6 nm for PTP-5 coating (Fig. 3h), indicated that the surface roughness of three coatings has insignificant difference. The XRD patterns (Fig. 3i) show that the β phase diffraction peak of P(VDF-TrFE) at 2θ = 19.8° and

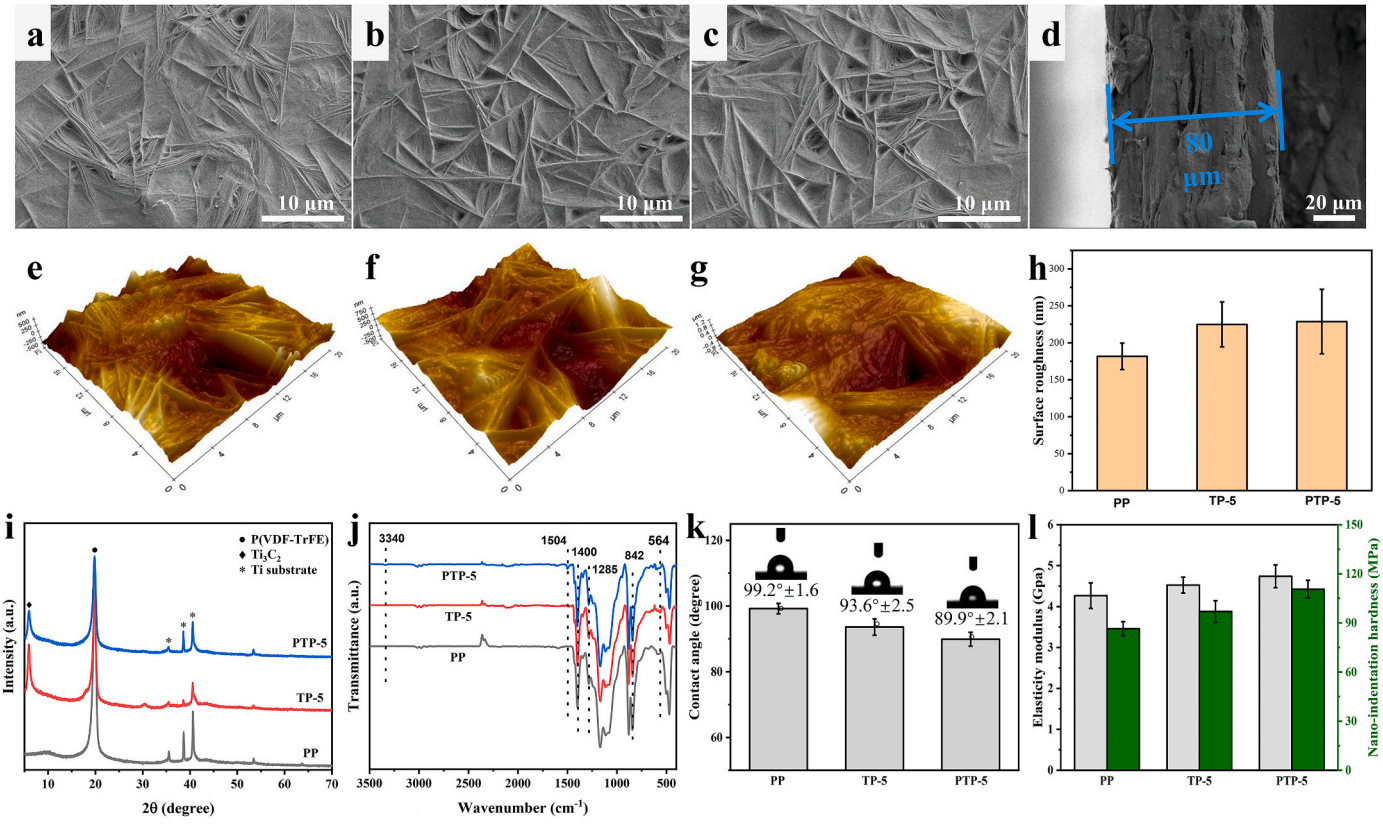

Fig. 3. SEM images of PP (a), TP-5 (b) and PTP-5 (c) coatings. SEM image of cross section of PTP-5 coating (d). AFM images of PP (e), TP-5 (f) and PTP-5 (g) coatings and surface roughness analysis (h). XRD patterns (i), FTIR spectra (j) and water contact angle (k), elasticity modulus and nano-indentation hardness (l) of PP, TP-5 and PTP-5 coatings.

diffraction peaks of Ti substrate at 2θ = 35.5°, 38.6° and 40.6° are found in PP, TP-5 and PTP-5 coatings, while a new diffraction peak at 2θ = 6.0° is emerged in TP-5 and PTP-5, which is indexed to the (002) crystal plane of the Ti_3C_2 nanosheets [38]. As observed in FTIR spectra (Fig. 3j), all the coating samples present three absorption bands of β phase of P (VDF-TrFE), with the absorption band at 1400 cm^{-1} assigned to the CH_2 wagging vibration, and the absorption bands at 1285 and 842 cm^{-1} ascribed to the CF_2 symmetric stretching vibration [39]. As expected, a characteristic absorption band at 564 cm^{-1} indexed to Ti–O bond of Ti_3C_2 is observed in TP-5 and PTP-5 coatings [40]. Compared with TP-5, a new absorption band at 1504 cm^{-1} is found in PTP-5 coating, which is assigned to the stretching vibration of C═N bond of PDA generated by self-polymerization of DA [33]. The measuring results of contact angle (Fig. 3k) show that all the coating samples exhibit hydrophobic characterization, and the water contact angle decreases slightly from PP, TP-5 to PTP-5, which is attributed that both the Ti_3C_2 and PDA are hydrophilic matter [41]. Moreover, the elasticity modulus and nano-indentation were measured to evaluate the nano-mechanical property of the coating samples. As shown in Fig. 3l, a slight increase in elasticity modulus of the coatings is obtained, with 4.27 ± 0.31 GPa for PP, 4.52 ± 0.19 GPa for TP-5 and 4.74 ± 0.28 GPa for PTP-5. And also, the nano-indentation of the coatings is also enhanced, in which the average nano-indentation of PP, TP-5 and PTP-5 coatings is determined to 86.5, 97.0 and 110.6 MPa, respectively. The increased elasticity modulus and nano-indentation in PTP-5 may be attributed that the NH_2 groups of in situ formed PDA on the surface of Ti_3C_2 can strongly interact with CF_2 groups of P(VDF-TrFE) through hydrogen bond interaction [42], which improved the interfacial bonding strength between hydrophobic P(VDF-TrFE) matrix and hydrophilic Ti_3C_2 nanofillers.

3.3. Adhesion strength, tribological and anti-corrosion properties of PTP nanocomposite coatings

In terms of implant coatings, the adhesion strength of coatings on substrates is one of the most key factors for its clinical application. A bioactive coating with low adhesion strength may be easily detached from substrate, which will destroy the inherent functionality of the coating. So, the adhesion strength of coating samples on Ti substrates was evaluated by nano-scratch test. It can be seen from Fig. 4a that all the coatings display clear deep scratch tracks with narrow at the beginning and wide at the end. Among, the scratch trace width of PTP-5 is visually narrower than that of PP and TP-5, maybe implying the stronger internal interaction and higher cohesion strength of PTP-5 coating. The magnified SEM images of scratch traces show that all the coatings are peeled off from Ti substrates at a certain position of respective scratch trace. It is well known that the critical load is considered as the adhesion strength of a coating on substrate [31]. According to the plot of normal load-scratch distance in Fig. 4b, the adhesion strength of PP, TP-5 and PTP-5 coatings is determined to 0.12, 0.14, 0.19 N. Compared with PP and TP-5 coatings, the adhesion strength of PTP-5 is enhanced by 58.3 % and 35.7 %, respectively. This can be ascribed that, on one hand, the DA adsorbed on the surface of Ti_3C_2 can be firmly adhered to the Ti substrate surface through the catechol chemistry during in situ polymerization process [43]; on the

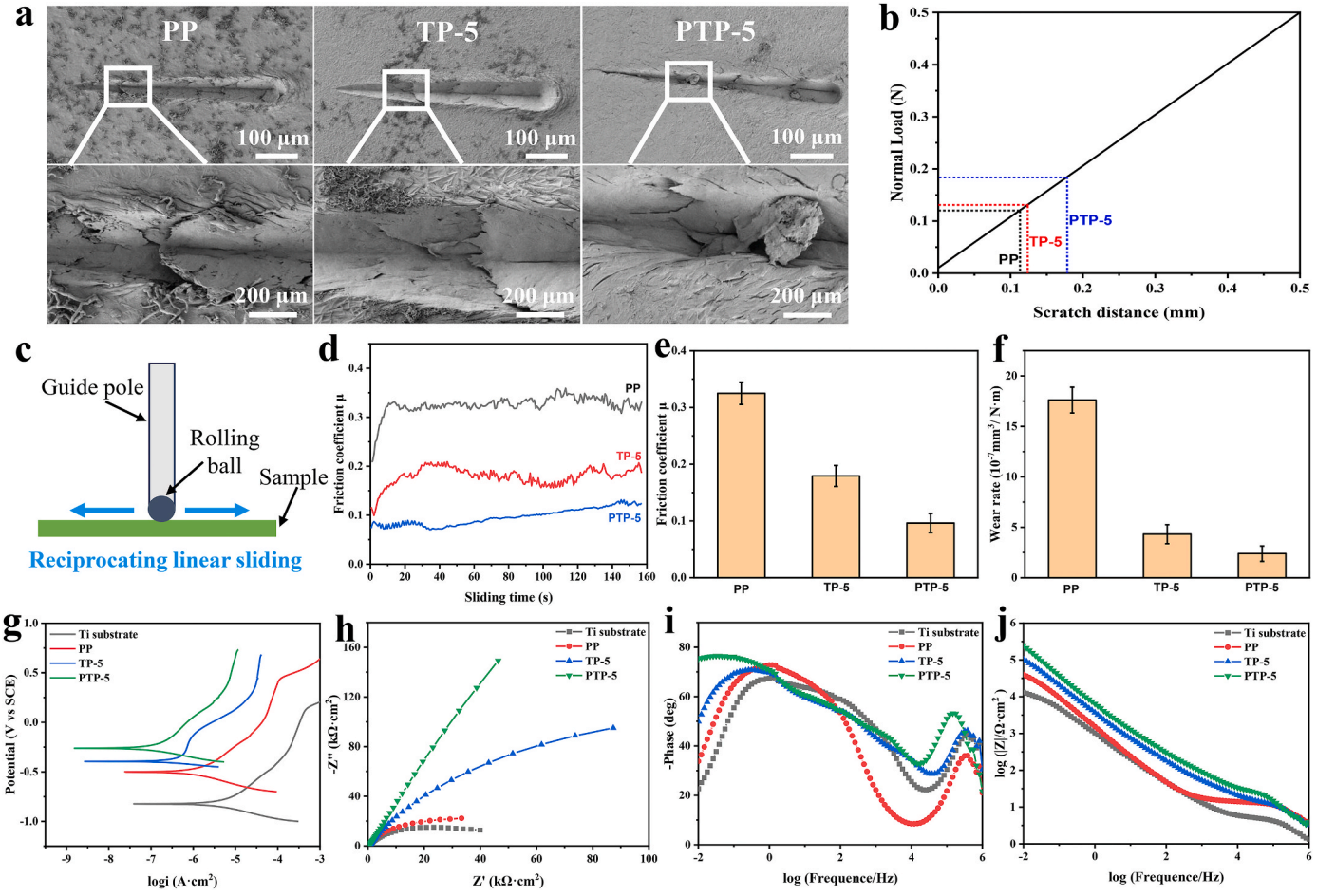

Fig. 4. SEM images of scratch traces on PP, TP-5 and PTP-5 coatings (a). The linear relation between scratch distance and normal load during nano-scratch test (b). Illustration for tribological performance test (c). Friction coefficient-sliding time curves (d), calculated friction coefficient (e) and wear rate (f) of PP, TP-5 and PTP-5 coatings. Tafel plots (g), Nyquist plots (h) and Bode-phase curves (i), Bode-impedance curves (j) of PP, TP-5 and PTP-5 coatings.

other hand, the in situ formed PDA improves the interfacial interactions between the Ti_3C_2 nanofillers and P(VDF-TrFE) substrate, which enhances the cohesion strength of PTP-5 coating, resulting in a stronger tearing resistance [44]. The tribological performance of implant surfaces is also a concern for clinical application. As illustrated in Fig. 4c, the tribological measurement of the coating samples was carried out by reciprocating linear sliding. Friction coefficient-time curves (Fig. 4d) display that a short running-in period (20–30 s) is observed at the beginning of friction process, and then the friction coefficient μ of all the coatings tends to become stabilized. Accordingly, the average friction coefficient of PP, TP-5 and PTP-5 coatings were calculated to 0.325, 0.179 and 0.096, respectively (Fig. 4e). Further, the calculated results in wear rate of the coatings show that, compared to PP coating, the wear rate of TP-5 and PTP-5 coatings is greatly decreased, and the PTP-5 coating obtained the lowest wear rate (Fig. 4f). It can be seen from Fig. S4, wear debris are observed on the wear mark of all the coatings, implying the abrasive wear mechanism in the friction process. Many large-sized wear debris are found on the wear mark of PP coating, however, the wear debris on the wear mark of PTP-5 coating is almost disappeared, indicating the optimal wear resistance in PTP-5 coating. The enhanced wear resistance in PTP-5 coating can be attributed to the enhanced nano-mechanical properties and reduced friction coefficient μ, which has been proved in Figs. 3l and 4e, respectively. Besides adhesion strength and tribological performance, the corrosion resistance of the coating plays a dominant role in the durability of the implant. Fig. 4g shows the typical potentiodynamic polarization curves (Tafel curves) of PP, TP-5 and PTP-5 coating on Ti substrates, and the corresponding E_{corr} and i_{corr} of these coatings are obtained by Tafel extrapolation method, as shown in Table 1. All the coatings present a similar Tafel curves with Ti substrate. Nevertheless, the E_{corr} of the samples shifts gradually towards the positive direction (Ti < PP < TP-5 < PTP-5) and the i_{corr} of the samples shifts gradually towards the negative direction (PTP-5 < TP-5 < PP < Ti). As a result, the inhibition efficiency of PP, TP-5 and PTP-5 are calculated to 67.0 %, 93.5 % and 97.7 %, respectively, which implies the PTP-5 coating possessed the best corrosion resistance against SBF solution. The EIS tests are further performed to investigate the interfacial charge transfer process between the samples and the electrolyte, and the results are presented by the Nyquist and Bode plots. It can be seen from Fig. 4h that the typical circular arc curves are observed in the Nyquist plots of each sample. It is well known that the diameter of a circular arc curve is closely related to the corrosion performance. Generally, the larger diameter represents the more difficult permeation of electrolytes into substrates, and directs the better corrosion resistance [45]. Obviously, the near-linear circular arc of the PTP-5 coating exhibits the largest diameter, revealing the best anticorrosion property of PTP-5 coating on Ti substrate. The Bode-phase plot (Fig. 4i) shows that the PTP-5 coating obtains a maximum phase angle near 80° at low frequency, indicating the excellent capacitive character in PTP-5/Ti sample, and the reduced maximum phase angle in other samples (Ti, PP, TP-5) maybe implies the occurrence of leakage phenomenon of capacitor [46]. Moreover, the highest resistance of PTP-5 coating in the Bode-impedance plot (Fig. 4j) also indicates the best anticorrosion property. This can be attributed that the PTP-5 coatings served as a physical barrier, making corrosive liquid difficult to reach the surface of the Ti substrate, and Ti_3C_2 reinforcing fillers could further enhance the barrier effect and impermeability of PTP-5 coating. Besides, the in situ formed PDA improved the interfacial bonding strength between P(VDF-TrFE) matrix and Ti_3C_2, resulting in fewer pores or gaps inside the coating, thereby enhancing the permeability resistance to the corrosive liquid.

Table 1
Electrochemical corrosion parameters of different samples in SBF solution.

Samples	E_{corr} (mV)	i_{corr} (A/cm^2)	Inhibition efficiency (%)
Ti	−823	3.48×10^{-6}	/
PP	−499	1.15×10^{-6}	67.0
TP-5	−395	2.26×10^{-7}	93.5
PTP-5	−261	7.96×10^{-8}	97.7

3.4. Photothermal property of PTP nanocomposite coatings

To further investigate the photothermal properties of the coating samples, a series of experiments were carried out in PBS solution under 808 nm NIR radiation. It can be seen from Fig. 5a, the temperature of the PTP-5 coating rises rapidly at first and then tend to be stabilized after ~2 min, and the ΔT at power densities of 100, 300 and 500 mW/cm^2 are determined to 4.8 °C, 9.5 °C and 19.6 °C, respectively. It is reported that mild thermal stimulation (ΔT: 3–5 °C) is beneficial to tissue repair and regeneration [47]. So, the power density of 100 mW/cm^2 was selected as NIR light source for subsequent studies. As shown in Fig. 5b, the ΔT of TP-5 coating is determined to 3.2 °C, which is significantly lower than that of PTP-5 coating. In addition, the PP coating exhibited an insignificant ΔT similar to PBS solution (negative control) after 10 min NIR irradiation at 100 mW/cm^2, indicating the negligible temperature change on PP coating. The infrared thermal images (Fig. 5c) further verify that the color change is quite remarkable in the TP-5 and PTP-5 coatings, while little color change is seen in the PP coating and PBS solution. The stability of photothermal effect of the PTP-5 coating was evaluated by conducting three ON/OFF cycles with 808 nm NIR of 100 mW/cm^2. As shown in Fig. 5d, the ΔT of PTP-5 coating is almost unchanged over three cycles, indicating the excellent photothermal stability of PTP-5 coating. It is important to note that the bone implants need to stay in the body for up to a year or even decades once implanted, which necessitates that the functional coating on the surface of the implant be able to maintain stable properties [48]. For example, if a bone implant has loosened after a few months (such as aseptic inflammation-induced bone loosening), an on-demand treatment can be implemented via the stable photothermal effect of the implant's surface coating. Although Ti_3C_2-based biomaterials show good photothermal performance in a short-term, their long-term photothermal performance may be drastically reduced considering that Ti_3C_2 can be gradually degraded in aqueous solution [49]. To evaluate the long-term photothermal stability, the photothermal heating curves of PTP-5 coating were examined under same conditions after soaked in PBS solution for six months. It can be seen from Fig. 5e that, compared with the freshly prepared PTP-5 coating, the ΔT of PTP-5 coating only shows a 5.9 % of reduction after six months, however, the ΔT of TP-5 coating has been reduced by 30.3 %. The long-term photothermal stability in PTP-5 coating is mainly ascribed that, on one hand, the in situ formed PDA improved the interfacial compatibility between Ti_3C_2 and P(VDF-TrFE), which makes it more difficult for SBF corrosive fluids to penetrate into the PTP-5 coating [50]; on the other hand , the encapsulation of PDA greatly reduced the contact between Ti_3C_2 nanosheets and SBF, which makes Ti_3C_2 nanosheets less susceptible to oxidation or degradation, thus allowing them to maintain their photothermal effect. The XRD pattern of PDA/Ti_3C_2 nanoparticles separated from the PTP-5 coating after six months showed that no diffraction peak of TiO_2 was observed (Fig. S5), confirming that the surface of the nanoparticles had not been oxidized.

3.5. Biological effects of photothermal PTP nanocomposite coatings on BMSCs

Since the optimal temperature for most mammalian cells in *ex vivo* culture is around 37 °C, the photothermal effect of the coating samples was re-examined under the environment of 37 °C before the biological experiment. The results showed that the ΔT with 37 °C as initial temperature is similar to the ΔT with 20 °C as initial temperature (Fig. S6), confirming the validity of ΔT in subsequent biological experiments. To assess the biocompatibility of the photothermal P(VDF-TrFE) nanocomposite coatings, the live/dead staining assays of BMSCs were

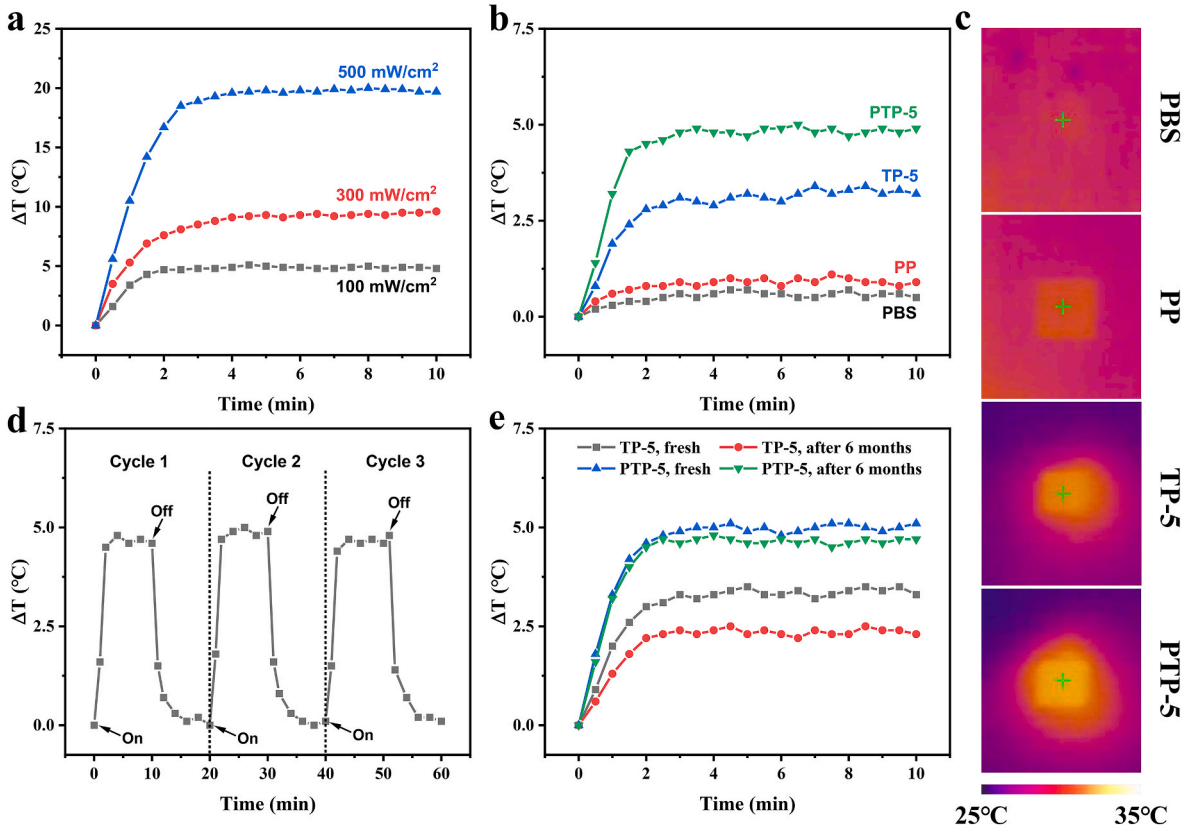

Fig. 5. Temperature change curves of PTP-5 coating under NIR irradiation at different power densities (a). Temperature change curves of PP, TP-5 and PTP-5 coatings under 100 mW/cm^2 NIR irradiation (b). Infrared thermal images of PBS solution, PP, TP-5 and PTP-5 coatings under 100 mW/cm^2 NIR irradiation (c). Recycling heating curves of PTP-5 coating under 100 mW/cm^2 NIR irradiation (d). Temperature change curves of TP-5 and PTP-5 at the time of freshly prepared and six months later (e).

performed under NIR irradiation (100 mW/cm^2). It can be seen from Fig. 6a, all the samples, including control, TP-5 and PTP-5 coating, exhibit the excellent biocompatibility under NIR (+) (with NIR irradiation) or NIR (−) (without NIR irradiation) after 2 days of culture, and the dead cells are scarcely observed in the visual field. The results of cell viability (Fig. 6b) show that no statistical difference is observed between different samples after 1, 3 and 7 days of culture. And also, the cell viability of BMSCs also shows insignificant differences in the same sample under NIR (+) or NIR (−). The cell morphology of BMSCs was further investigated by Rhodamine-Phalloidin kits. As shown in Fig. 6c, the cell spreading of BMSCs on PTP-5 coating is better than that on TP-5 coating and control under NIR (−) after culturing for 2 days, maybe ascribed to the adhesion promoting effect of PDA [51]. When NIR irradiation was implemented, the F-actin staining area (red) of BMSCs on TP-5 and PTP-5 coatings seem to be wider. Statistical analysis (Fig. 6d–f) shows that the BMSCs cultured on PTP-5 coating achieve the largest cell area, perimeter and feret's diameter under NIR (−), and the cell area, perimeter and feret's diameter of BMSCs are further enhanced under NIR (+), which indicates that the mild thermal stimulation on PTP-5 coating promoted the cell spreading of BMSCs effectively. Generally, the better cell spreading is more conducive to subsequent cell growth and osteogenic differentiation [52].

3.6. Osteogenic ability of BMSCs on photothermal PTP nanocomposite coatings

To further evaluate the osteogenic ability of the photothermal P(VDF-TrFE) nanocomposite coatings, the ALP and alizarin red staining assays were performed. It can be seen from ALP staining images (Fig. 7a) that the PTP-5 coating presents a larger ALP staining area than that of TP-5 and control under NIR (−), and the ALP staining area on both TP-5 and PTP-5 coatings are further enlarged under NIR (+), which is confirmed by the quantitative results of ALP staining images (Fig. 7b). The mineralization degree of BMSCs was investigated by alizarin red staining assay (Fig. 7c). Similarly, the larger staining areas are observed on the TP-5 and PTP-5 coatings under NIR (+), and the staining area on PTP-5 coating is obviously larger than that on TP-5 coating, which is also verified by quantitative results of alizarin staining images (Fig. 7d). The ALP and alizarin red staining results indicate that the NIR-induced mild thermal stimulus promotes the ALP activity and mineralization degree of BMSCs, and the stronger mild thermal stimulus can produce a better promoting effect of osteogenic differentiation. Besides ALP activity and cell mineralization, the expression level of OPN, RUNX-2 and OCN, which was usually used for assessing cellular osteogenic differentiation, were also analyzed by western blotting assays. As shown in Fig. 7e–h, the expression of OPN, RUNX-2 and OCN in TP-5+NIR and PTP-5+NIR were higher than those in other NIR (−) groups. There were no significant differences in the relative protein expression levels of OPN, RUNX-2 and OCN among different samples without NIR irradiation. However, the relative protein expression level of all the proteins is noticeably upregulated on the TP-5 and PTP-5 coatings with NIR irradiation, and the PTP-5+NIR group has the highest expression of osteogenic related proteins. Moreover, the OPN immunofluorescent staining assay was carried out for further investigate the osteogenic ability. Fig. 7i displays the representative fluorescence images of cell nucleus (blue) and OPN (green). Apparently, the fluorescence intensity of OPN on TP-5 and PTP-5 coatings with NIR irradiation is much higher than that on other samples, proving the pro-osteogenic effect of mild thermal stimulus again. The quantified results (Fig. S7) reveal that the fluorescence intensity of OPN on PTP-5 coating is significantly higher than that on TP-5

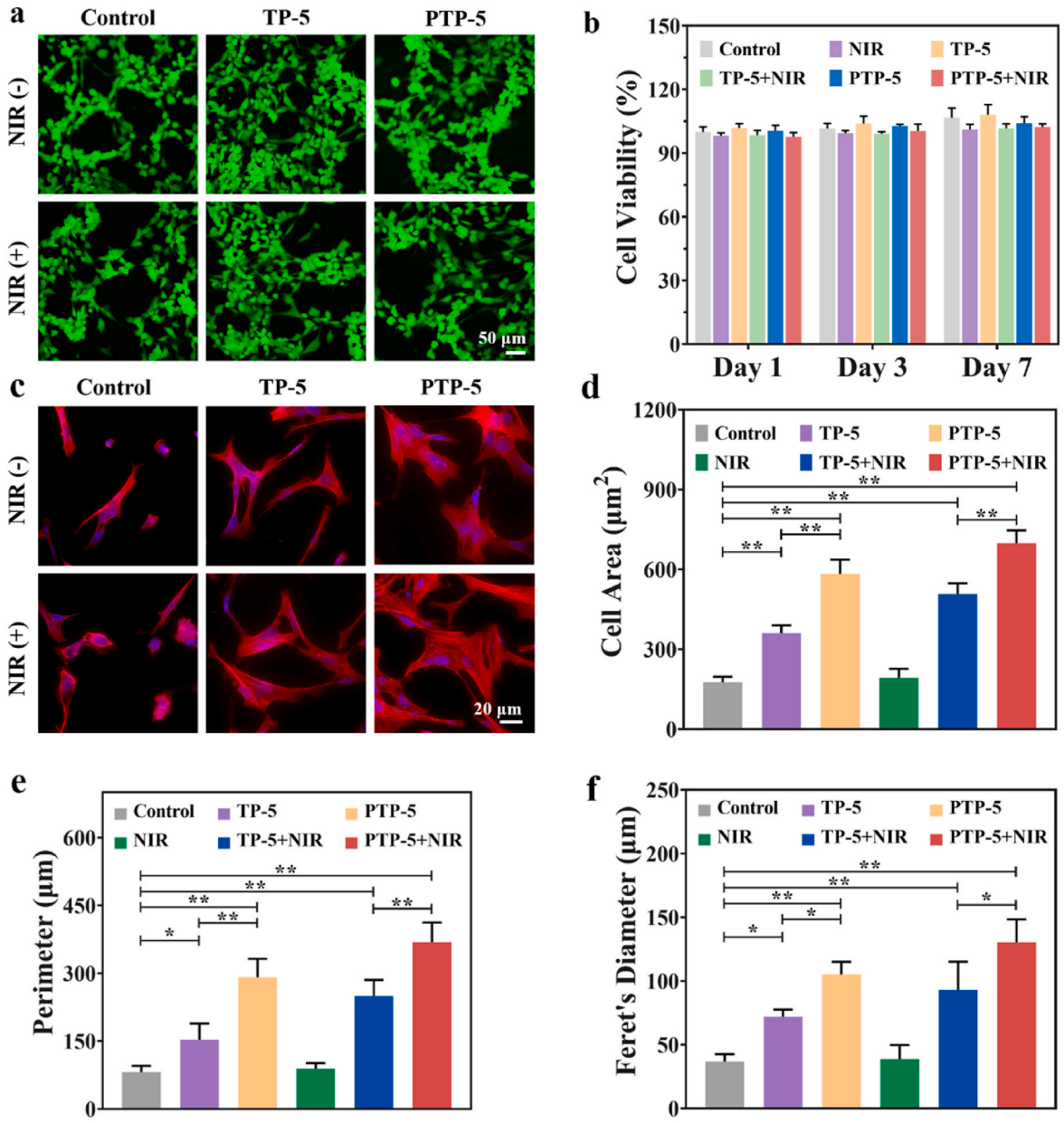

Fig. 6. Fluorescence images of live/dead staining of BMSCs cultured on different samples with or without NIR irradiation after 2 days (a). Cell viability at 1, 3, and 7 days (b). Representative images of cytoskeleton staining of BMSCs (c). Quantification of cell area (d), perimeter (e) and ferret's diameter (f) of BMSCs.

coating.

3.7. Osteogenic mechanism on photothermal PTP nanocomposite coatings

It is well known that cell differentiation strongly depends on the surface characteristics of biomaterials. In the process of cells attaching onto the surface of biomaterial, cells are able to sense the surface microenvironment, such as surface roughness, electrical charge and temperature [53], and subsequently establishing the specific binding between cell surface integrins and ECM proteins adsorbed on the biomaterial surface. As an important physical characteristic, temperature plays a critical role in cell growth behaviors, including cellular adhesion, differentiation, apoptosis, and so on [54]. It is reported that the thermal stimulation (temperature variation) of biomaterial surface can strongly induce the synthesis of heat shock protein (HSP) that is a class of ubiquitous heat stress proteins from bacteria to mammals, and then effecting the subsequent cell responses [55]. Many previous works found that the expression level of HSP47 (a kind of key HSP) was significantly upregulated at the same time of achievement of pro-osteogenesis under thermal stimulation [8,56,57]. Nagata group [58] further proved that the HSP47 was a molecular chaperone protein of collagen and was able to promote the early synthesis and maturation of COL-I. As is well known, COL-I is the main component of ECM proteins and plays a positive role in cell differentiation. Previous studies have shown that cell integrins composed of β1 and different α subunits, such as α1β1, α2β1, α5β1, have been usually implicated into the cell-material interactions through binding with ECM proteins [59]. For instance, the specific recognition and binding between integrin α5β1 and fibronectin of ECM produced a significant promoting effect in cell adhesion and osteogenic differentiation [60]. In our previous work, we have demonstrated that, among different cell integrins including α1β1, α2β1, α5β1 and αvβ1, the specific binding between integrin α2β1 and COL-I is responsible for the enhanced cellular osteogenic differentiation through activating the α2β1-mediated MEK/ERK signaling pathway

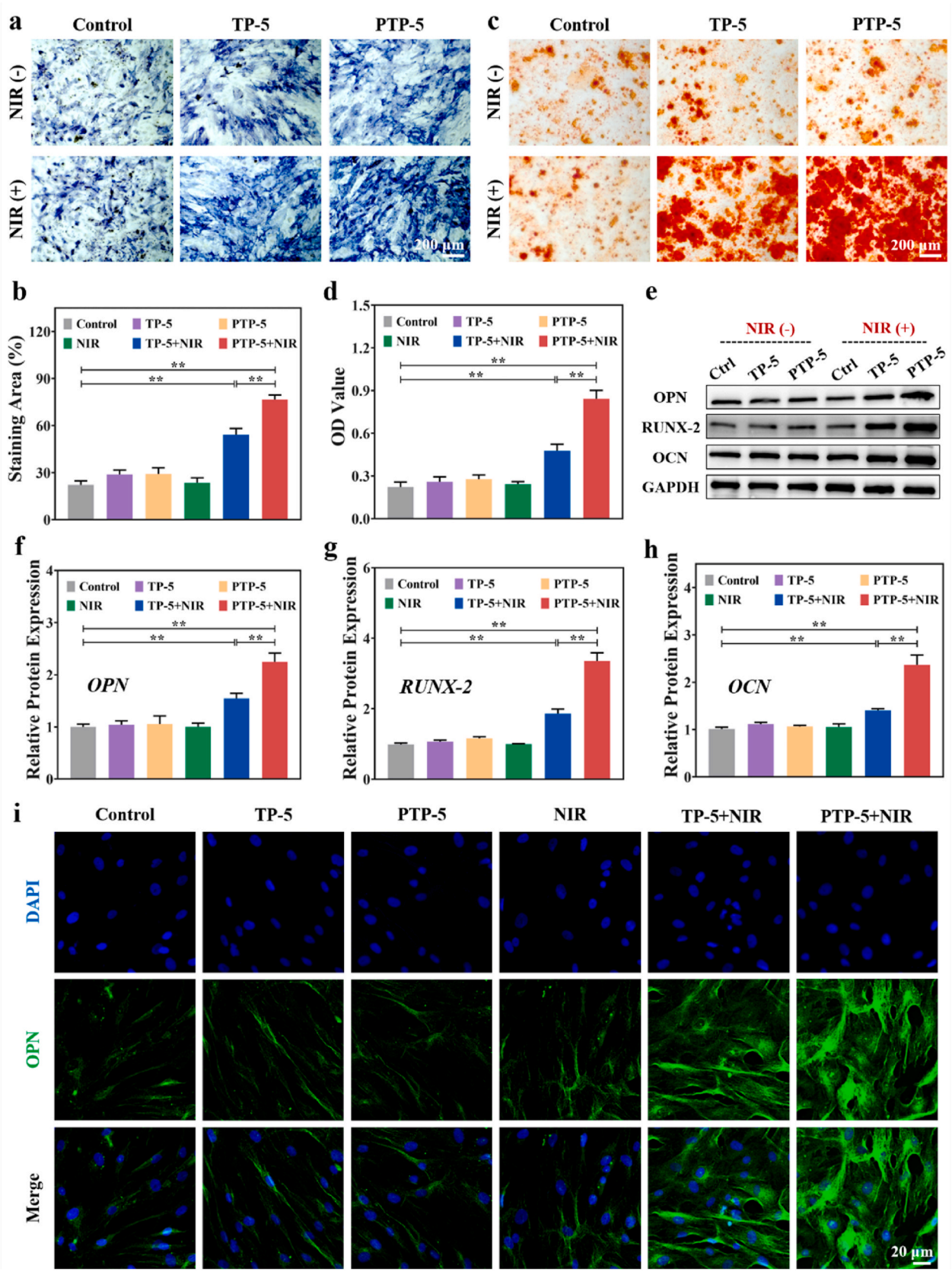

Fig. 7. ALP staining images (a) and quantification of staining area (b) of BMSCs after culturing for 7 days. Alizarin red staining images (c) and quantification of mineralization capacity (d) of BMSCs after culturing for 21 days. The representative image of western blotting (e) and the relative protein expression level of OPN, RUNX-2 and OCN (f–h). GAPDH was the reference. (i) The representative images of the BMSCs after immunofluorescent staining (Blue: cell nuclei; Green:OPN).

[61]. So, it is speculated that the HSP-COL-I interaction and α2β1-mediated MEK/ERK signaling pathway maybe play dominating role in mild thermal stimulation driven osteogenesis.

To investigate the underlying osteogenic mechanism under mild thermal stimulation, some key signaling proteins including HSP-47, COL-I, integrin α2, integrin β1, *p*-MEK (phosphorylated MEK) and *p*-ERK (phosphorylated ERK) were analyzed by western blotting assay. As shown in Fig. 8a, the expression of each protein in PTP-5+NIR group seemed to be the highest. The quantification of protein bands (Fig. 8b–g) shows that the relative expression level of all the proteins (HSP-47, COL-I, α2, β1, *p*-MEK and *p*-ERK) of TP-5 and PTP-5 coating is markedly upregulated when NIR irradiation was implemented. And also, the relative expression level of the related proteins of PTP-5 coating is much higher than that of TP-5 coating, which may be attributed to the higher ΔT on PTP-5 coating. Previous researches demonstrated that the mild thermal stimulation (ΔT: 3–5 °C) could promote osteogenesis, and within this suitable ΔT range, the higher ΔT exhibited the better pro-osteogenic effect [47,62]. Concerning the current results, it is thought that the MEK/ERK signaling pathway is likely responsible for the improvement of mild thermal stimulation induced osteogenic differentiation. In order to further verify the possible MEK/ERK osteogenic signaling pathway, the inhibition assays were performed with PTP-5+NIR group by adding the inhibitor U0126 into the cell culture medium. Results show that the addition of U0126 inhibits the ALP secretion (Fig. 8h) and mineralization degree (Fig. 8i) of BMSCs. Besides, the expression level of osteogenesis-related markers (OPN, RUNX-2 and OCN) were also strongly inhibited, as observed in Fig. 8j and k. These results clearly revealed the dominating role of MEK/ERK signaling pathway in mild thermal stimulation induced osteogenic differentiation. Based on the abovementioned results and analysis, a plausible mechanism is proposed for enhanced cellular osteogenic differentiation on the photothermal P(VDF-TrFE) nanocomposite coatings, as illustrated in Fig. 8l. When NIR is illuminated on the surface of photothermal coatings, the HSP47 is inductively synthesized due to the mild thermal stimulation. Whereafter, the thermal induced HSP47 specifically recognizes and binds with the triple helix structured tropocollagen of COL-I via hydrophobic-hydrophilic interactions, which prevents the COL-I from biological inactivation caused by the unfoldment or aggregation of the tropocollagen, thereby promoting the self-assembly synthesis and maturation of COL-I [58,63]. As a result, the expression level of integrin α2β1 is also upregulated with the increase of COL-I content due to the specific recognition and binding between α2β1 and COL-I. The enhanced specific α2β1-COL-I interaction promoted the expression of downstream *p*-MEK and *p*-ERK signaling proteins in the integrin α2β1-mediated MEK/ERK signaling pathway, thereby improving the cellular osteogenic differentiation.

3.8. Regulation of macrophage polarization by photothermal PTP nanocomposite coatings

In addition, the immunoregulation dominated by macrophages also plays a vital role in the repair and regeneration of injured tissue. As is known to all, macrophages can be polarized to the M1 or M2 phenotypes depended on the surrounding microenvironment [64]. M1 phenotype mainly secretes proinflammatory cytokines that induce inflammatory response and retard tissue regeneration, and M2 phenotype mainly secretes anti-inflammatory cytokines that attenuate inflammatory response and accelerate tissue healing [65–67]. Among them, M2 macrophages are thought to be effective in stimulating the differentiation of BMSCs into mature osteoblasts and stimulating bone mineralization in vitro [68]. This is due to the fact that bone morphogenetic protein 2, transforming growth factor-β and insulin-like growth factor 1 secreted by M2 macrophages can induce osteoblast differentiation [69]. To understand the effect of the photothermal P(VDF-TrFE) nanocomposite coatings on the polarization behaviors of macrophages, the representative proinflammatory and anti-inflammatory cytokines of macrophages were examined by immunofluorescence staining, western blotting and enzyme-linked immunosorbent assays. The immunofluorescent staining images in Fig. 9a show that the fluorescence intensity of proinflammatory iNOS of macrophages cultured on TP-5 and PTP-5 coatings reduces significantly after NIR irradiation is applied, while the fluorescence intensity of anti-inflammatory Arg-1 increases, which is further confirmed by the quantified results of fluorescence images (Fig. 9b and c) and protein bands of western blotting (Fig. 9d–f). Moreover, the results of enzyme-linked immunosorbent assay (ELISA) also show that the illumination of NIR on TP-5 and PTP-5 coatings inhibits the secretion of proinflammatory TNF-α and iNOS, but promotes the secretion of anti-inflammatory Arg-1 and IL-10 greatly (Fig. 9g–j). These results indicated that mild thermal stimulation on TP-5 and PTP-5 coatings can induce the M2 polarization of macrophages, which is consistent with the research results of Li et al. [14]. The possible reasons mainly be attributed that the mild thermal stimulation upregulated the expression of heat shock proteins, such as HSP47, which can inhibit the expression of NF-κB, thereby decreasing the secretion of inflammatory factors [16,24]. Noting that, when NIR irradiation is not applied, the expression of proinflammatory cytokines has the following order: control > TP-5 > PTP-5 (Fig. 9b–e,g,h), while the expression of anti-inflammatory cytokines has opposite order (Fig. 9c–f,i,j), implying the higher degree of M2 polarization of macrophages on PTP-5 coating, which may be attributed the good antioxidant ability of PDA and Ti_3C_2 in the PTP-5 [70,71], as proved by the in vitro and *vivo* ROS scavenging assays. Results show that both the Ti_3C_2 and PDA/Ti_3C_2 nanoparticles present good free radical scavenging capability against $\cdot O_2^-$, ·OH and DPPH· radicals under NIR (−), and a higher scavenging ratio is gained in the PDA/Ti_3C_2 (Figs. S8a–c). For the coating samples, the scavenging ratio of three free radicals has the same order: PP < TP-5 < PTP-5 under NIR (−), and the NIR-triggered thermal stimulation has insignificant effect on the free radical scavenging capability of the same group sample. Furthermore, the cellular reactive oxygen species (ROS) level (green fluorescence) of PTP-5 coating under NIR (−) is lower than that of TP-5 and control under NIR (−) after incubation for 30 min, but the NIR-triggered thermal stimulation has no influence on cellular ROS level (Figs. S8d and e). The in vitro and *vivo* ROS scavenging assays indicated that the stronger antioxidant ability of PTP-5 coating mainly depended on the chemical composition of PDA and Ti_3C_2. Based on these results, it is speculated that NIR-triggered thermal stimulation and antioxidant components (PDA and Ti_3C_2) may promoted M2 polarization of macrophages on the PTP-5 coating together.

3.9. Antibacterial activity of PTP nanocomposite coatings

Bacterial infection at the site of material implantation is one of the key factors that hinder bone tissue repair and regeneration [72,73]. Therefore, the antibacterial activity of PTP nanocomposite coatings under NIR (+) or NIR (−) was assessed by the spread plate and bacterial live/dead staining tests. In spread plate test, the bacterial colonies of both *S. aureus* (Fig. 10a) and *E. coli* (Fig. 10b) among three samples show no difference after 24 h of incubation under NIR (−). When NIR was illuminated for 10 min, the bacterial colonies of TP-5 and PTP-5 coatings reduces dramatically, and the bacterial colonies of *S. aureus* and *E. coli* treated with PTP-5 coating are visibly less than that treated with TP-5 coating. Nevertheless, no significant change is observed in bacterial colonies of control group. Furthermore, the bacterial live/dead staining images show that almost no dead *S. aureus* (Fig. 10c) and *E. coli* (Fig. 10d) bacterium are observed on three samples under NIR (−). After NIR irradiation for 10 min, the live bacteria numbers on control group did not seem to decrease significantly, however, almost all the *S. aureus* and *E. coli* bacterium on TP-5 and PTP-5 coatings are killed. The quantified results of bacterial live/dead staining images show that the bacteria reduction rate of *S. aureus* (Fig. 10e) and *E. coli* (Fig. 10f) on PTP-5 coatings reached up to 99.38 % and 99.44 %, respectively. This is ascribed that the NIR-triggered high temperature (> 45 °C) can damage

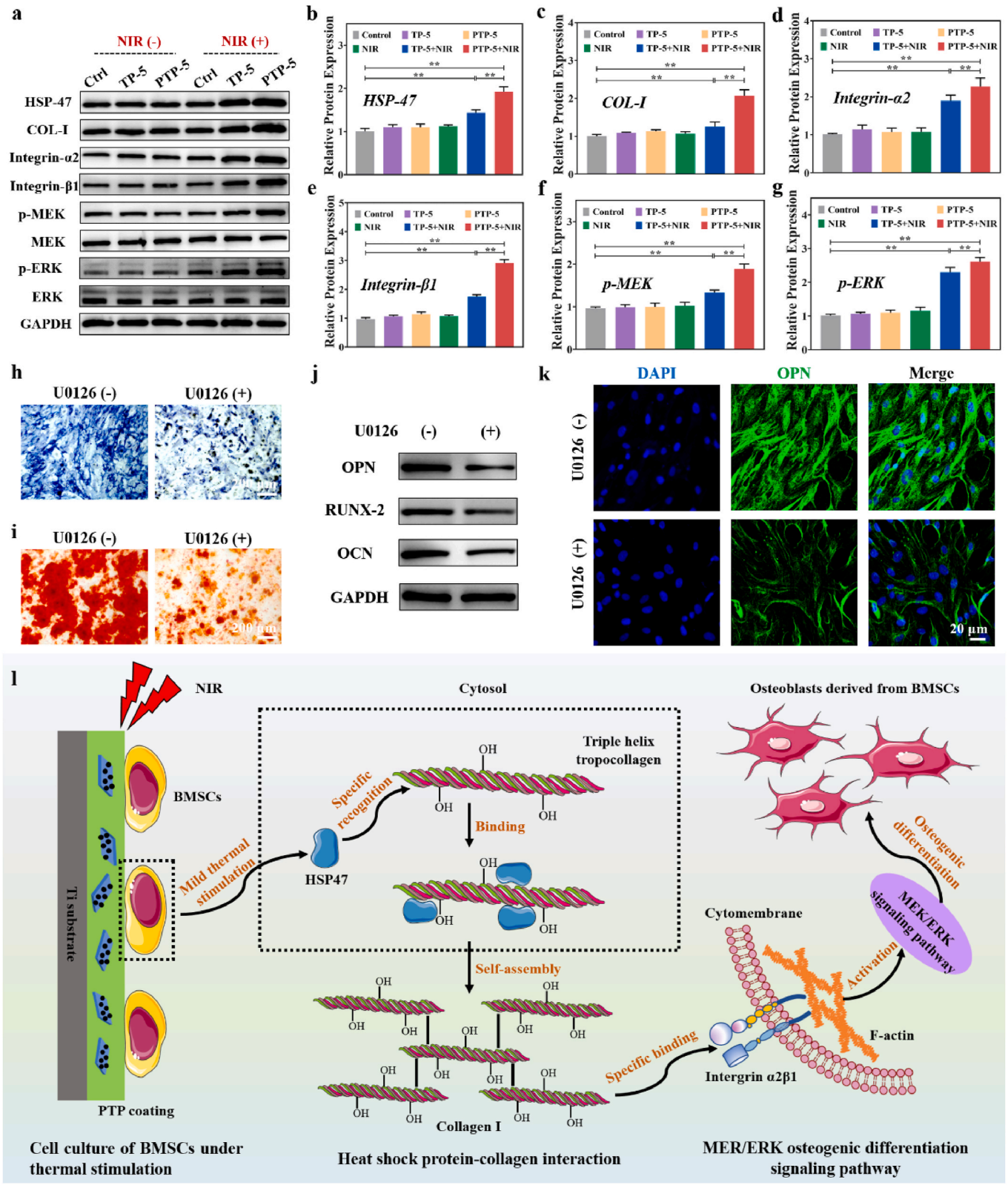

Fig. 8. Representative images of western blotting analysis (a) and the relative protein expression level of HSP-47, COL-I, Integrin-α2, Integrin-β1, *p*-MEK and *p*-ERK (b–g). GAPDH was the reference. ALP (h) and alizarin red (i) staining images of BMSCs with the addition of inhibitor U0126. Western blotting images of OPN, RUNX-2 and OCN proteins with the addition of inhibitor U0126 using GAPDH as reference (j). Representative immunofluorescent staining images of OPN protein of the BMSCs with the addition of inhibitor U0126 (k). Schematic diagram of the underlying mechanism for mild photothermal stimulation driven osteogenic differentiation (l).

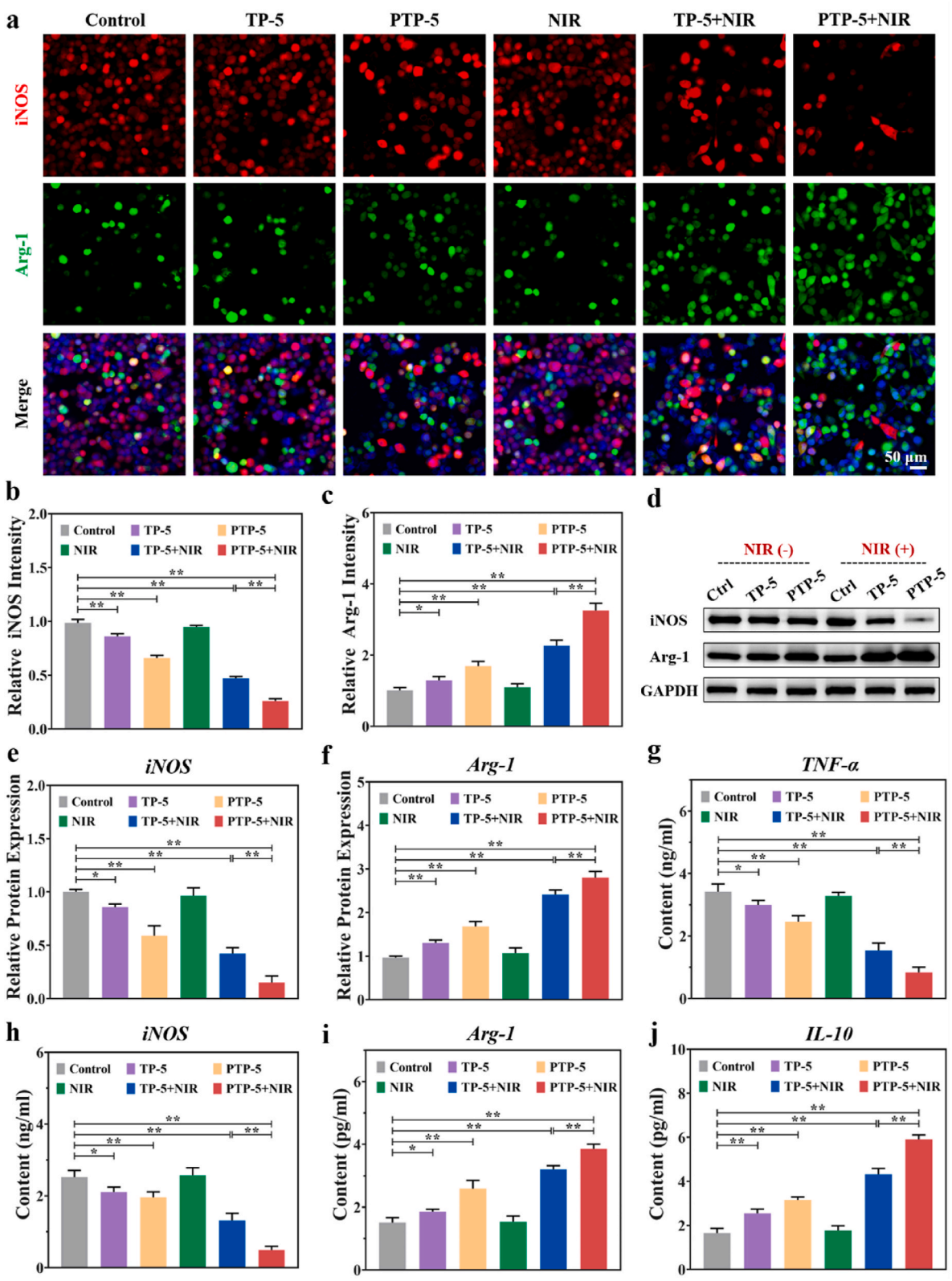

Fig. 9. Immunofluorescent staining and merged images of iNOS (red) and Arg-1 (green) cytokines of macrophages (a). The relative fluorescence intensity of iNOS (b) and Arg-1 (c). Protein bands of western blotting (d) and the relative protein expression level of iNOS (e) and Arg-1 (f). GAPDH was the reference. The content of the secreted TNF-α (g), iNOS (h), Arg-1 (i) and IL-10 (j) cytokines of macrophages.

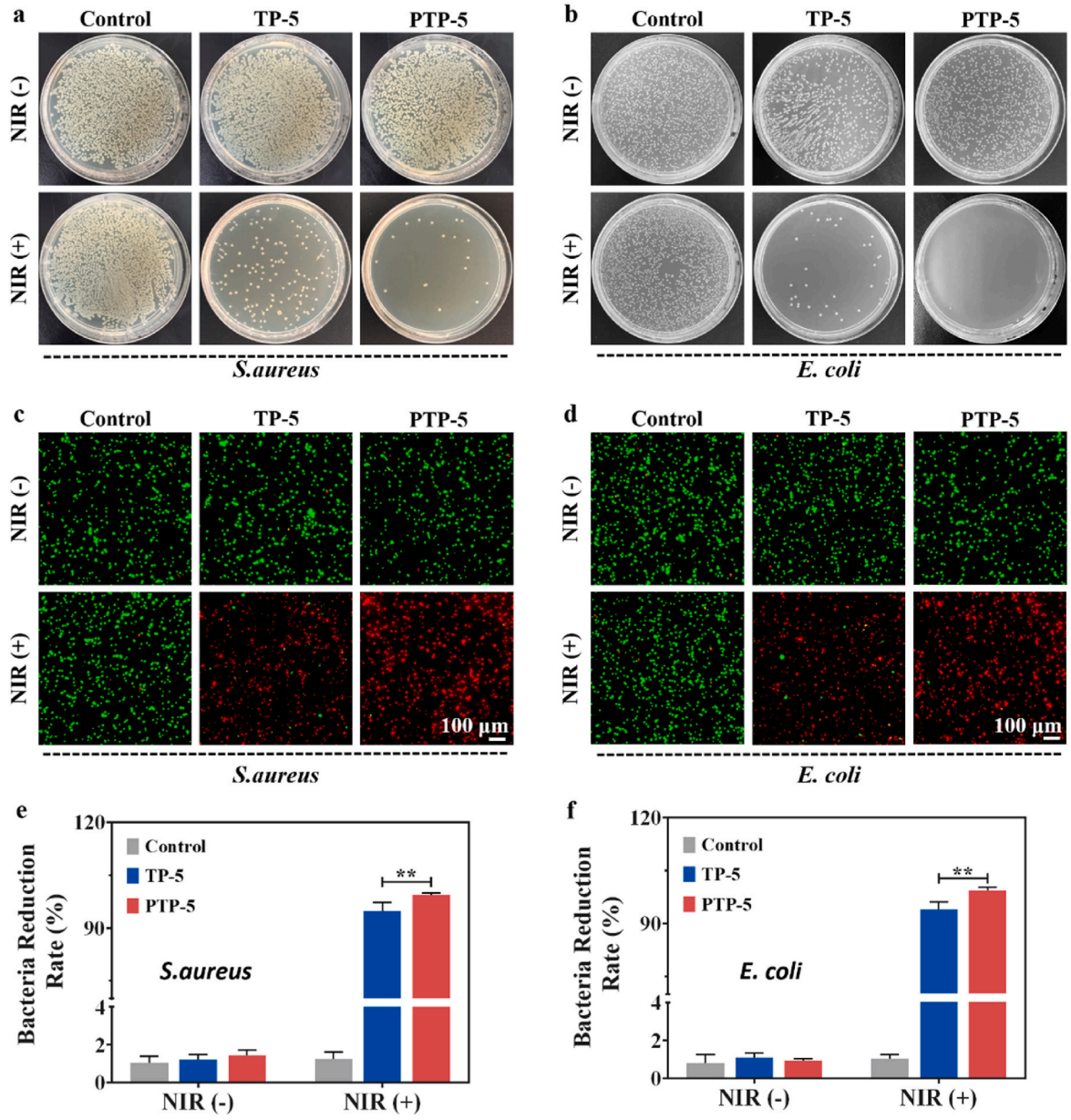

Fig. 10. Photographs of the bacterial colonies of *S. aureus* (a) and *E. coli* (b) after 24 h of incubation with different coating samples under NIR (+) or NIR (−). Bacterial live/dead staining images (c,d) and bacteria reduction rate (e,f) of *S. aureus* and *E. coli* incubated with different samples under NIR (+) or NIR (−).

cell membrane of bacteria and denature the bacterial enzymes, thereby inducing bacterial death, which has been widely proved by previous publications [74–76].

4. Conclusions

In summary, a bioactive PDA/Ti_3C_2/P(VDF-TrFE) nanocomposite coating with NIR-triggered photothermal effect was developed for accelerating bone tissue repair and regeneration. The in situ polymerization of dopamine in P(VDF-TrFE) matrix endow this coating high adhesion strength on Ti substrate, excellent tribological and corrosion resistance properties, which may meet the clinical requirements of implant coating. More importantly, the in situ polymerized PDA could improve the interfacial compatibility between Ti_3C_2 nanofillers and P(VDF-TrFE) matrix, which enhanced the photothermal property of PDA/Ti_3C_2/P(VDF-TrFE) coating. The mild thermal stimulation triggered by NIR on the coating promoted the synthesis of HSP, enhancing the specific interaction between HSP and ECM proteins, thereby activating the integrin-mediated MEK/ERK osteogenic differentiation signaling pathway. In addition, the mild thermal stimulation on the coatings promoted the expression of anti-inflammatory Arg-1 and IL-10 cytokines and included polarization of macrophages towards M2 phenotype, which is conductive to create a favorable microenvironment for accelerating bone regeneration. Thanks to excellent photothermal performance, the bacteria reduction rate of both *S. aureus* and *E. coli*. on the PTP-5 coating were more than 99 %, exhibiting the excellent antibacterial activity. Thus, we believe that our newly prepared and multifunctional bioactive coatings have great potential in the field of bone repair.

CRediT authorship contribution statement

Sanqiang Xia: Writing – original draft, Methodology, Investigation, Data curation. **Dun Liu:** Writing – review & editing, Visualization, Supervision, Conceptualization. **Kanling Jiang:** Methodology, Investigation, Data curation. **Miao Cao:** Visualization, Investigation, Formal

analysis, Data curation. **Zhenqi Lou:** Software, Project administration, Formal analysis. **Ruobing Cheng:** Visualization, Validation, Project administration, Investigation. **Jie Yi:** Software, Resources, Investigation, Data curation. **Anlin Yin:** Validation, Software, Resources, Project administration. **Yi Jiang:** Visualization, Resources, Project administration, Funding acquisition. **Kui Cheng:** Writing – review & editing, Validation, Supervision, Resources, Funding acquisition. **Wenjian Weng:** Writing – review & editing, Validation, Supervision, Resources, Funding acquisition. **Benlong Shi:** Writing – review & editing, Supervision, Resources, Funding acquisition, Formal analysis, Conceptualization. **Bolin Tang:** Writing – review & editing, Supervision, Resources, Project administration, Funding acquisition, Conceptualization.

Declaration of competing interest

We submit the manuscript entitled "Photothermal driven BMSCs osteogenesis and M2 macrophage polarization on polydopamine-coated Ti_3C_2 nanosheets/poly(vinylidene fluoride trifluoroethylene) nanocomposite coatings" for consideration for publication as a Research Paper in Materials Today Bio. No conflict of interest exits in the submission of this manuscript, and manuscript is approved by all authors for publication. I would like to declare on behalf of my co-authors that the work described was original research that has not been published previously, and not under consideration for publication elsewhere, in whole or in part. All the authors listed have approved the manuscript that is enclosed.

Data availability

No data was used for the research described in the article.

Acknowledgements

This work is financially supported by National Natural Science Foundation of China (No. 32271373, 82302685, 51902135 and 52101385), the Zhejiang Provincial Natural Science Foundation of China (No. LY22E020013), the Jiaxing Youth Science and Technology Talent Project (No. 2023AY40018), the Jiaxing Public Welfare Research Project (2024AD10056) and the First Hospital of Jiaxing/The Affiliated Hospital of Jiaxing University Joint Fund (No. 2022LHJJ003).

Appendix A. Supplementary data

Supplementary data to this article can be found online at https://doi.org/10.1016/j.mtbio.2024.101156.

References

[1] D. Tang, R.S. Tare, L.Y. Yang, D.F. Williams, K.L. Ou, R.O. Oreffo, Biofabrication of bone tissue: approaches, challenges and translation for bone regeneration, Biomaterials 83 (2016) 363–382.
[2] J. Li, L. Qin, K. Yang, Z. Ma, Y. Wang, L. Cheng, D. Zhao, Materials evolution of bone plates for internal fixation of bone fractures: a review, J. Mater. Sci. Technol. 36 (2020) 190–208.
[3] Y. Yu, G. Jin, Y. Xue, D. Wang, X. Liu, J. Sun, Multifunctions of dual Zn/Mg ion co-implanted titanium on osteogenesis, angiogenesis and bacteria inhibition for dental implants, Acta Biomater. 49 (2017) 590–603.
[4] O. Geuli, N. Metoki, N. Eliaz, D. Mandler, Electrochemically driven hydroxyapatite nanoparticles coating of medical implants, Adv. Funct. Mater. 26 (44) (2016) 8003–8010.
[5] K. Ikuta, H. Urakawa, E. Kozawa, S. Hamada, T. Ota, R. Kato, H. Honda, T. Kobayashi, N. Ishiguro, Y. Nishida, In vivo heat-stimulus-triggered osteogenesis, Int. J. Hyperther. 31 (1) (2015) 58–66.
[6] J. Chen, Z.D. Shi, X. Ji, J. Morales, J. Zhang, N. Kaur, S. Wang, Enhanced osteogenesis of human mesenchymal stem cells by periodic heat shock in self-assembling peptide hydrogel, Tissue Eng. 19 (5–6) (2013) 716–728.
[7] C. Shui, A. Scutt, Mild heat shock induces proliferation, alkaline phosphatase activity, and mineralization in human bone marrow stromal cells and Mg-63 cells in vitro, J. Bone Miner. Res. 16 (4) (2010) 731–741.
[8] X. Zhang, G. Cheng, X. Xing, J. Liu, Y. Cheng, T. Ye, Q. Wang, X. Xiao, Z. Li, H. Deng, Near-infrared light-triggered porous AuPd alloy nanoparticles to produce mild localized heat to accelerate bone regeneration, J. Phys. Chem. Lett. 10 (15) (2019) 4185–4191.
[9] S. Li, S. Chien, P.I. Brånemark, Heat shock-induced necrosis and apoptosis in osteoblasts, J. Orthop. Res. 17 (6) (1999) 891–899.
[10] S. Sayed, O. Faruq, M. Hossain, S.B. Im, Y.S. Kim, B.T. Lee, Thermal cycling effect on osteogenic differentiation of MC3T3-E1 cells loaded on 3D-porous Biphasic Calcium Phosphate (BCP) scaffolds for early osteogenesis, Mater. Sci. Eng., C 105 (2019) 110027.
[11] R.J. Miron, D.D. Bosshardt, OsteoMacs: key players around bone biomaterials, Biomaterials 82 (2016) 1–19.
[12] R. Klopfleisch, Macrophage reaction against biomaterials in the mouse model-Phenotypes, functions and markers, Acta Biomater. 43 (2016) 3–13.
[13] T.D. Smith, R.R. Nagalla, E.Y. Chen, W.F. Liu, Harnessing macrophage plasticity for tissue regeneration, Adv. Drug Deliv. Rev. 114 (2017) 193–205.
[14] B. Li, F. Liu, J. Ye, X. Cai, R. Qian, K. Zhang, Y. Zheng, S. Wu, Y. Han, Regulation of macrophage polarization through periodic photo-thermal treatment to facilitate osteogenesis, Small 18 (38) (2022) e2202691.
[15] H. Wang, X. Zeng, L. Pang, H. Wang, B. Lin, Z. Deng, E.L.X. Qi, N. Miao, D. Wang, P. Huang, H. Hu, J. Li, Integrative treatment of anti-tumor/bone repair by combination of MoS_2 nanosheets with 3D printed bioactive borosilicate glass scaffolds, Chem. Eng. J. 396 (2020) 125081.
[16] B. Xu, Z. Li, Q. Ye, G. Li, M. Xu, Y. Li, L. Liu, W. Song, Y. Zhang, Mild photothermal effect of titania nanotubes array as a promising solution for peri-implantitis, Mater. Des. 217 (2022) 110641.
[17] Y. Chen, W. Liu, S. Wan, H. Wang, Y. Chen, H. Zhao, C. Zhang, K. Liu, T. Zhou, L. Jiang, Q. Cheng, X. Deng, Superior synergistic osteogenesis of MXene-based hydrogel through supersensitive drug release at mild heat, Adv. Funct. Mater. 34 (2) (2024) 2309191.
[18] L. Tong, Q. Liao, Y. Zhao, H. Huang, A. Gao, W. Zhang, X. Gao, W. Wei, M. Guan, P. K. Chu, H. Wang, Near-infrared light control of bone regeneration with biodegradable photothermal osteoimplant, Biomaterials 193 (2019) 1–11.
[19] U. Yadav, H. Mishra, V. Singh, S. Kashyap, A. Srivastava, S. Yadav, P.S. Saxena, Enhanced osteogenesis by molybdenum disulfide nanosheet reinforced hydroxyapatite nanocomposite scaffolds, ACS Biomater. Sci. Eng. 5 (9) (2019) 4511–4521.
[20] B. Tang, B. Zhang, J. Zhuang, Q. Wang, L. Dong, K. Cheng, W. Weng, Surface potential-governed cellular osteogenic differentiation on ferroelectric polyvinylidene fluoride trifluoroethylene films, Acta Biomater. 74 (2018) 291–301.
[21] Z. Wang, X. He, B. Tang, X. Chen, L. Dong, K. Cheng, W. Weng, Polarization behavior of bone marrow-derived macrophages on charged P(VDF-TrFE) coatings, Biomater. Sci. 9 (3) (2021) 874–881.
[22] W. Liu, F. Zhang, Y. Yan, C. Zhang, H. Zhao, B.C. Heng, Y. Huang, Y. Shen, J. Zhang, L. Chen, X. Wen, X. Deng, Remote tuning of built-in magnetoelectric microenvironment to promote bone regeneration by modulating cellular exposure to arginylglycylaspartic acid peptide, Adv. Funct. Mater. 31 (6) (2021) 2006226.
[23] J. Nunes-Pereira, S. Ribeiro, C. Ribeiro, C.J. Gombek, S. Lanceros-Méndez, Poly (vinylidene fluoride) and copolymers as porous membranes for tissue engineering applications, Polym. Test. 44 (2015) 234–241.
[24] Q. Li, W. Wang, H. Feng, L. Cao, H. Wang, D. Wang, S. Chen, NIR-triggered photocatalytic and photothermal performance for sterilization based on copper sulfide nanoparticles anchored on $Ti_3C_2T_x$ MXene, J. Colloid Interface Sci. 604 (2021) 810–822.
[25] B.P. Lee, P.B. Messersmith, J.N. Israelachvili, J.H. Waite, Mussel-inspired adhesives and coatings, Annu. Rev. Mater. Res. 41 (2011) 99–132.
[26] R. Zheng, S. Wang, Y. Tian, X. Jiang, D. Fu, S. Shen, W. Yang, Polydopamine-coated magnetic composite particles with an enhanced photothermal effect, ACS Appl. Mater. Interfaces 7 (29) (2015) 15876–15884.
[27] Q. Zeng, Y. Qian, Y. Huang, F. Ding, X. Qi, J. Shen, Polydopamine nanoparticle-dotted food gum hydrogel with excellent antibacterial activity and rapid shape adaptability for accelerated bacteria-infected wound healing, Bioact. Mater. 6 (9) (2021) 2647–2657.
[28] Y. Liu, H. Meng, Z. Qian, N. Fan, W. Choi, F. Zhao, B.P. Lee, A moldable nanocomposite hydrogel composed of a mussel-inspired polymer and a nanosilicate as a fit-to-shape tissue sealant, Angew. Chem., Int. Ed. 56 (15) (2017) 4224–4228.
[29] B. Tang, Y. Yang, Y. Shi, H. Nie, H. Xia, X. Shen, Improved mechanical performances of short aramid fiber-reinforced polypropylene composites by Ti_3C_2 Mxene nanosheets, Polym. Compos. 42 (4) (2021) 2010–2018.
[30] W.C. Oliver, G.M. Pharr, An improved technique for determining hardness and elastic modulus using load and displacement sensing indentation experiments, J. Mater. Res. 7 (1992) 1564–1583.
[31] M.H. Lin, Y.H. Wang, C.H. Kuo, S.F. Ou, P.Z. Huang, T.Y. Song, Y.C. Chen, S. T. Chen, C.H. Wu, Y.H. Hsueh, F.Y. Fan, Hybrid ZnO/chitosan antimicrobial coatings with enhanced mechanical and bioactive properties for titanium implants, Carbohyd. Polym. 257 (2021) 117639.
[32] Z. Zhang, M. Yang, J. Yuan, F. Guo, X. Men, Friction and wear behaviors of MoS_2-multi-walled-carbonnanotube hybrid reinforced polyurethane composite coating, Friction 7 (4) (2019) 316–326.
[33] R.A. Zangmeister, T.A. Morris, M.J. Tarlov, Characterization of polydopamine thin films deposited at short times by autoxidation of dopamine, Langmuir 29 (27) (2013) 8619–8628.
[34] X. Yang, D. Wang, J. Zhu, L. Xue, C. Ou, W. Wang, M. Lu, X. Song, X. Dong, Functional black phosphorus nanosheets for mitochondria-targeting photothermal/photodynamic synergistic cancer therapy, Chem. Sci. 10 (13) (2019) 3779–3785.

[35] Y. Chen, Y. Jiang, W. Feng, W. Wang, D. Yu, Construction of sensitive strain sensing nanofibrous membrane with polydopamine-modified MXene/CNT dual conductive network, Colloid. Surface. 635 (2022) 128055.

[36] X. Du, J. Wang, L. Jin, S. Deng, Y. Dong, S. Lin, Dopamine-decorated $Ti_3C_2T_x$ MXene/cellulose nanofiber aerogels supported form-stable phase change composites with superior solar-thermal conversion efficiency and extremely high thermal storage density, ACS Appl. Mater. Interfaces 14 (13) (2022) 15225–15234.

[37] C. Sen, S. Qianru, L. Hui, In situ growth of gold nanoparticles onto polydopamine-modified MXene to quickly and efficiently degrade dyes, J. Mater. Sci. (2023) 1026–1043.

[38] M. Alhabeb, K. Maleski, B. Anasori, P. Lelyukh, L. Clark, S. Sin, Y. Gogotsi, Guidelines for synthesis and processing of two-dimensional titanium carbide ($Ti_3C_2T_x$ MXene), Chem. Mater. 29 (18) (2017) 7633–7644.

[39] W. Liu, H. Zhao, C. Zhang, S. Xu, F. Zhang, L. Wei, F. Zhu, Y. Chen, Y. Chen, Y. Huang, M. Xu, Y. He, B.C. Heng, J. Zhang, Y. Shen, X. Zhang, H. Huang, L. Chen, X. Deng, In situ activation of flexible magnetoelectric membrane enhances bone defect repair, Nat. Commun. 14 (1) (2023) 4091.

[40] W.T. Cao, F.F. Chen, Y.J. Zhu, Y.G. Zhang, Y.Y. Jiang, M.G. Ma, F. Chen, Binary strengthening and toughening of MXene/cellulose nanofiber composite paper with nacre-inspired structure and superior electromagnetic interference shielding properties, ACS Nano 12 (5) (2018) 4583–4593.

[41] B. Zhu, P. Song, J. Li, S. Cao, J. Shi, Ti_3C_2 MXene/gold nanorods-based hybrid nanoparticles with photodynamic antibacterial activities, J. Mater. Sci. 57 (42) (2022) 19957–19971.

[42] T. Li, M. Qu, C. Carlos, L. Gu, F. Jin, T. Yuan, X. Wu, J. Xiao, T. Wang, W. Dong, X. Wang, Z.Q. Feng, High-performance poly(vinylidene difluoride)/dopamine core/shell piezoelectric nanofiber and its application for biomedical sensors, Adv. Mater. 33 (3) (2021) e2006093.

[43] F. Ponzio, J. Barthès, J. Bour, M. Michel, P. Bertani, J. Hemmerlé, M. d'Ischia, V. Ball, Oxidant control of polydopamine surface chemistry in acids: a mechanism-based entry to superhydrophilic-superoleophobic coatings, Chem. Mater. 28 (13) (2016) 4697–4705.

[44] L. Han, X. Lu, K. Liu, K. Wang, L. Fang, L.T. Weng, H. Zhang, Y. Tang, F. Ren, C. Zhao, G. Sun, R. Liang, Z. Li, Mussel-inspired adhesive and tough hydrogel based on nanoclay confined dopamine polymerization, ACS Nano 11 (3) (2017) 2561–2574.

[45] A. Ray, I. Mukhopadhyay, R. Pati, Y. Hattori, U. Prakash, Y. Ishii, S. Kawasaki, Optimization of photoelectrochemical performance in chemical bath deposited nanostructured CuO, J. Alloys Compd. 695 (2017) 3655–3665.

[46] X. He, G. Zhang, X. Wang, R. Hang, X. Huang, L. Qin, B. Tang, X. Zhang, Biocompatibility, corrosion resistance and antibacterial activity of TiO_2/CuO coating on titanium, Ceram. Int. 43 (18) (2017) 16185–16195.

[47] J. Zhang, Y. Wang, N. Ding, P. Ma, Z. Zhang, Y. Liu, Photothermal regulation of macrophage polarization with 2D $Ti_3C_2T_x$ MXene nanosheets for enhanced immunomodulatory osteogenesis, Colloid Interface Sci. 56 (2023) 100733.

[48] J. Raphel, M. Holodniy, S.B. Goodman, S.C. Heilshorn, Multifunctional coatings to simultaneously promote osseointegration and prevent infection of orthopaedic implants, Biomaterials 84 (2016) 301–314.

[49] John Chuanfang, Sergio Zhan, Niall Pinilla, Conor McEvoy, P. Cullen, Oxidation stability of colloidal two-dimensional titanium carbides (MXenes), Chem. Mater. 29 (11) (2017) 4848–4856.

[50] X. He, J. Wu, Y. Chen, L. Zhang, X. Sheng, A trace amount of MXene@PDA nanosheets for low-temperature zinc phosphating coatings with superb corrosion resistance, Appl. Surf. Sci. 603 (2022) 154455.

[51] Y.L. Cheng, Y.W. Chen, K. Wang, M.Y. Shie, Enhanced adhesion and differentiation of human mesenchymal stem cell inside apatite-mineralized/poly(dopamine)-coated poly(ε-caprolactone) scaffolds by stereolithography, J. Mater. Chem. B 4 (38) (2016) 6307–6315.

[52] J. Pärssinen, H. Hammarén, R. Rahikainen, V. Sencadas, C. Ribeiro, S. Vanhatupa, S. Miettinen, S. Lanceros-Méndez, V.P. Hytönen, Enhancement of adhesion and promotion of osteogenic differentiation of human adipose stem cells by poled electroactive poly(vinylidene fluoride), J. Biomed. Mater. Res. 103 (3) (2015) 919–928.

[53] W.L. Murphy, T.C. McDevitt, A.J. Engler, Materials as stem cell regulators, Nat. Mater. 13 (6) (2014) 547–557.

[54] C.P. Ye, B.C. Heng, H. Liu, W.S. Toh, T. Cao, Culture media conditioned by heat-shocked osteoblasts enhances the osteogenesis of bone marrow-derived mesenchymal stromal cells, Cell Biochem. Funct. 25 (3) (2007) 267–276.

[55] M.P. Mayer, B. Bukau, Hsp70 chaperones: cellular functions and molecular mechanism, Cell. Mol. Life Sci. 62 (6) (2005) 670–684.

[56] K. Ma, C. Liao, L. Huang, R. Liang, J. Zhao, L. Zheng, W. Su, Electrospun PCL/MoS_2 nanofiber membranes combined with NIR-triggered photothermal therapy to accelerate bone regeneration, Small 17 (51) (2021) e2104747.

[57] Y. Zhao, X. Peng, D. Wang, H. Zhang, Q. Xin, M. Wu, X. Xu, F. Sun, Z. Xing, L. Wang, P. Yu, J. Xie, J. Li, H. Tan, C. Ding, J. Li, Chloroplast-inspired scaffold for infected bone defect therapy: towards stable photothermal properties and self-defensive functionality, Adv. Sci. 9 (31) (2022) e2204535.

[58] S. Ito, K. Nagata, Roles of the endoplasmic reticulum-resident, collagen-specific molecular chaperone Hsp47 in vertebrate cells and human disease, J. Biol. Chem. 294 (6) (2019) 2133–2141.

[59] I. Guryanov, S. Fiorucci, T. Tennikova, Receptor-ligand interactions: advanced biomedical applications, Mater. Sci. Eng., C 68 (2016) 890–903.

[60] T. Miller, D. Boettiger, Control of intracellular signaling by modulation of fibronectin conformation at the cell-materials interface, Langmuir 19 (5) (2003) 1723–1729.

[61] B. Tang, X. Shen, Y. Yang, Z. Xu, J. Yi, Y. Yao, M. Cao, Y. Zhang, H. Xia, Enhanced cellular osteogenic differentiation on $CoFe_2O_4$/P(VDF-TrFE) nanocomposite coatings under static magnetic field, Colloids Surf., B 198 (2021) 111473.

[62] Y. Kong, J. Duan, F. Liu, L. Han, G. Li, C. Sun, Y. Sang, S. Wang, F. Yi, H. Liu, Regulation of stem cell fate using nanostructure-mediated physical signals, Chem. Soc. Rev. 50 (22) (2021) 12828–12872.

[63] T. Ono, T. Miyazaki, Y. Ishida, M. Uehata, K. Nagata, Direct in vitro and in vivo evidence for interaction between Hsp47 protein and collagen triple helix, J. Biol. Chem. 287 (9) (2012) 6810–6818.

[64] L. Lv, Y. Xie, K. Li, T. Hu, X. Lu, Y. Cao, X. Zheng, Unveiling the mechanism of surface hydrophilicity-modulated macrophage polarization, Adv. Healthcare Mater. 7 (19) (2018) e1800675.

[65] T.A. Wynn, K.M. Vannella, Macrophages in tissue repair, regeneration, and fibrosis, Immunity 44 (3) (2016) 450–462.

[66] X.G. Yu, S.J. Jiang, D.J. Li, S.G. Shen, X.D. Wang, K.L. Lin, Osteoimmunomodulatory bioinks for 3D bioprinting achieve complete regeneration of critical-sized bone defects, Compos. Part B-Eng. 273 (2024) 111256.

[67] H.P. Wei, J.J. Cui, K.L. Lin, J. Xie, X.D. Wang, Recent advances in smart stimuli-responsive biomaterials for bone therapeutics and regeneration, Bone Res 10 (2022) 1–17.

[68] Z.W. Zheng, Y.H. Chen, D.Y. Wu, J.B. Wang, M.M. Lv, X.S. Wang, J. Sun, Z. Y. Zhang, Development of an accurate and proactive immunomodulatory strategy to improve bone substitute material-mediated osteogenesis and angiogenesis, Theranostics 8 (19) (2018) 5482–5500.

[69] L. Gong, Y. Zhao, Y. Zhang, Z. Ruan, The macrophage polarization regulates MSC osteoblast differentiation in vitro, Ann. Clin. Lab. Sci. 46 (1) (2016) 65–71.

[70] J. Liu, W. Lu, X. Lu, L. Zhang, H. Dong, Y. Li, Versatile $Ti_3C_2T_x$ MXene for free-radical scavenging, Nano Res. 15 (3) (2022) 2558–2566.

[71] I. Zarkesh, F. Movahedi, H. Sadeghi-Abandansari, S. Pahlavan, M. Soleimani, H. Baharvand, ROS scavenging activity of polydopamine nanoparticle-loaded supramolecular gelatin-based hydrogel promoted cardiomyocyte proliferation, Int. J. Biol. Macromol. 259 (2) (2024) 129228.

[72] M.U. Joshi, S.P. Kulkarni, M. Choppadandi, M. Keerthana, G. Kapusetti, Current state of art smart coatings for orthopedic implants: a comprehensive review, Smart Mater. Med. 4 (2023) 661–679.

[73] J.K. Zhang, Y. Zhuang, R.L. Sheng, H. Tomás, J. Rodrigues, G.Y. Yuan, X.D. Wang, K.L. Lin, Smart stimuli-responsive strategies for titanium implant functionalization in bone regeneration and therapeutics, Mater. Horiz. 11 (2024) 12–36.

[74] X. Chen, Y.Q. Gao, Y.L. Wang, G.Q. Pan, Mussel-inspired peptide mimicking: an emerging strategy for surface bioengineering of medical implants, Smart Mater. Med. 2 (2021) 26–37.

[75] X.X. Zhan, J.L. Yan, D. Xiang, H. Tang, L.L. Cao, Y.F. Zheng, H. Lin, D.D. Xia, Near-infrared light responsive gold nanoparticles coating endows polyetheretherketone with enhanced osseointegration and antibacterial properties, Mater. Today Bio 25 (2024) 100982.

[76] X.C. Kang, P.F. Guan, C.R. Xiao, C. Liu, Y.J. Guan, Y.Y. Lin, Y. Tian, K.Y. Ren, Y. T. Huang, R.M. Fu, C.Y. Ning, L. Fan, G.X. Tan, L. Zhou, Injectable intrinsic photothermal hydrogel bioadhesive with on-demand removability for wound closure and MRSA-infected wound healing 13 (12) (2023) 2203306.